異方性SnO_2のガス応答に対する焼成温度の効果

梅, ウンテイ
九州大学総合理工学府物質理工学専攻

Calcination Temperature Effect of Anisotropic SnO_2 Nanorods on Gas Response

(異方性 SnO_2 のガス応答に対する焼成温度の効果)

学生番号　2ES19128T

氏名　梅　ウンテイ　印

指導教員氏名　島江憲剛　印

提出日　2021 年 2 月 10 日

Contents

Contents ····· i

Chapter 1. **Introduction** ····· 1

1.1.Introduction ····· 1

1.2. Semiconductor gas sensor ····· 1

1.2.1. Semiconductor gas sensor based on SnO_2 ····· 1

1.2.2. Gas sensing mechanism ····· 4

1.2.3. Oxygen adsorption species on the surface of the device ····· 6

1.3. Key Factors of Oxide Semiconductor Gas Sensor ····· 8

1.3.1. Receptor function ····· 8

1.3.2. Transducer function ····· 9

1.3.3. Utility factor ····· 13

1.4. Reaction site ····· 15

1.4.1. Introduction ····· 15

1.4.2. Function of exposed crystal faces ····· 16

1.4.3. Method for controlling the exposed crystal faces ····· 18

1.5. Motivation ····· 19

Chapter 2. **Preparation** ····· 21

2.1. Introduction ·····21

2.2. Synthesis of SnO_2 solution by using the hydrothermal treatment ·····21

2.3. Material evaluation ·····24

2.3.1. X-ray diffraction (XRD) method and fundamental parameter (FP) method ·····24

2.3.2. Observation by Transmission Electron Microscope(TEM) ·····24

2.3.3 Observation by Field Emission Scanning Electronic Microscopy (FE-SEM) ·····24

2.3.4 Specific surface area and pore distribution by BET method ·····24

2.3.5 Observation of sensor element film thickness with a laser microscope···25

2.4. Preparation of sensor experimental device ·····25

2.4.1. Preparation of device ·····25

2.4.2. Preparation of measuring device ·····25

2.4.3. Measuring method ·····29

2.4.4. Pore size distribution ·····29

2.5. Summary·····30

Chapter 3. **Evaluation of anisotropic SnO_2 nanoparticles** ·····31

3.1. Introduction ·····31

3.2. Characteristics of SnO_2 nanoparticles ·····31

3.2.1. X-ray diffraction patterns ·····31

3.2.2. Pore size and surface area of SnO_2 by BET method ·····33

3.2.3. Morphology evaluation by FE-SEM ····· 34

3.2.4. Morphology evaluation by TEM ····· 39

3.2.5 Observation of sensor film thickness ····· 41

3.3. Summary ····· 41

Chapter 4. **Effect of anisotropy of SnO_2 nanoparticles on sensor characteristics**

4.1. Introduction ····· 42

4.2. Sensor characterization of SnO_2 ····· 42

4.3. Gas response of different gas molecule sizes ····· 43

4.4. Gas response of gases with different reaction pathways ····· 47

4.5. The effect of calcination temperature on sensor characteristics ····· 49

4.5.1. Gas response of SnO_2 calcined at different temperature to H_2 ····· 49

4.5.2. Gas response of SnO_2 calcined at different temperature to Ethanol ····· 49

4.6. Summary ····· 51

Chapter 5. **Conclusions** ····· 53

Acknowledgements ····· 55

References ····· 56

Chapter 1.

Introduction

1.1 Introduction

Japan in the 1960s reached high economic growth, and a large amount of pollutants were emitted due to increased traffic demand and production activities, and imports of household LP gas began. At that time, inflammable gas leakage and carbon monoxide poisoning occurred frequently, which became a serious social problem[1]. The problem reached a turning point in 1962. Semiconductor gas sensors using metal oxide semiconductors were discovered separately by Seiyama et al. and Taguchi et al. In 1962, Seiyama et al. reported that the adsorption or desorption of gas on the surface of the ZnO film gas sensor [2] could change the conductivity of the material. On the other hand, Taguchi et al. reported the change in electrical resistance due to the oxidation reaction in the SnO_2 sintered gas sensor [3]. In 1968, Figaro Engineering Co., Ltd. released the first semiconductor-type flammable gas sensor as a commercial product [4]. Since the gas leak alarm detects one digit or less of the lower limit of the explosion of inflammable gas, it will detect several thousand ppm. In the case of CO, it is necessary to detect at the level of several ppm to sub ppm. Since then, various gas sensors have been reported. Among them, tin oxide is often used as a material because of chemical stability and catalytic activity, so it can detect inflammable gases with high sensitivity and long-term stability. However, SnO_2-based semiconductor gas sensors are required to have higher sensitivity detection for low-concentration gases, improved selectivity, and suppression of the influence of water vapor. Nowadays, researchers are making a lot of efforts to reduce the effects of pollutants, and gas sensors are not only widely used from industrial to consumer use, it is also the most basic link of the IoT (Internet of Things) and a bridge between various information and artificial intelligence. Gas sensors used in many fields[5] such as functional materials, electronic ceramics, optoelectronic components, MEMS technology [6][7], nanotechnology, and organic polymers. High-performance gas sensors can greatly improve the level of information collection, processing, and deep processing, improve the accuracy of real-time prediction of accidents, continue to eliminate hidden accidents, and greatly reduce accidents, especially major accidents. It can effectively realize "electronization" of safety supervision and safety production supervision and

management, change passive disaster relief into active disaster prevention, and advance safety production to scientific management[8].

In recent years, "sick house syndrome" and Japan's aging society have progressed[9], and the needs to detect air pollution caused by paints and building materials in homes and VOC gas in exhaled breath has expanded, and the ability of gas sensor to detect ppb or sub-ppb levels will be required.

1.2 Semiconductor gas sensor

1.2.1. Semiconductor gas sensor based on SnO_2

The semiconductor gas sensor detects gas using an oxide semiconductor, and detects gas by changing the electric conductivity when the test gas comes into contact with the oxide semiconductor. There are two types of semiconductor gas sensors, electrical resistance type and non-electric resistance type. Furthermore, there are two types of electrical resistance type: one in which the interaction with gas changes the electrical resistance (surface control type) and the other in which the defect structure change due to the reaction between bulk and gas changes the electrical resistance (bulk control type). Generally, the sensor sensitivity of an electric resistance change type gas sensor is defined as Ra / Rg (Ra: electric resistance value in air, Rg: electric resistance value in test gas).

The SnO_2 gas sensor used in this study is classified as a surface control type. The surface control type sensor detects the gas by utilizing the change in the electric resistance value when the gas is adsorbed on the semiconductor surface or reacts on the semiconductor surface. Table 1.1 shows the classification of semiconductor gas sensors. The surface-controlled semiconductor gas sensor has the advantages of a simple sensor structure, gas detection sensitivity (in some cases, gas on the order of ppm can be detected), and a high sensor response speed, and research and development was carried out from the earliest. Currently, the main research subjects as surface-controlled semiconductor gas sensor materials are SnO_2 and ZnO. This is because it exhibits relatively high stability in both an oxidizing atmosphere and a reducing atmosphere at a temperature of 500°C or less. Furthermore, considering the gas adsorption performance, the n-type semiconductor has a larger amount of gas adsorption than the n-type semiconductor for the electron-withdrawing gas such as O_2, and it becomes an electron-

Table 1.1 Classification of semiconductor gas sensors. [10]

Type	Physical characteristics	Materials	Operating Temperature	Typical target gas
surface control type	Electrical conductivity	SnO_2, ZnO	Room temperature-450°C	Flammable gas
	Surface potential	Ag_2O	Room temperature	Mercabtan
	Rectification characteristics (diode)	Pd/CdS, Pd/TiO_2	Room temperature-200°C	H_2, CO, Ethanol
	Threshold voltage (Transistor)	Pd gate MOSFET	150°C	H_2, H_2S
bulk control type	Electrical conductivity	$La_{1-x}Sr_xCoO_3$, γ-Fe_2O_3	300°C-450°C	Ethanol, Flammable gas
		TiO_2, CoO-MgO, SnO_2	700°C or more	O_2

donating gas such as H_2 and CO. On the other hand, it is said that the amount of gas adsorbed by n-type semiconductors is larger than that of p-type semiconductors. Further,

Table 1.2 Application example of the gas sensor.[11][12]

Safety Applications	Indoor Air Quality/HVAC Applications	Medical and Health Applications	Transportation Applications	Industrial Applications
Ensure safety for · Beverage industries · Factories · Vehicles	Monitor air quality · Homes · Office buildings · Air conditioner.	· Medical breath diagnostic machine · alcohol checker · Gas analyzer	Monitor gas concentrations in enclosed environments to know how to prolong perishable goods	Monitor extreme environments · Industrial gases · Various environmental measurements

the flammable gas is considered to react with the adsorbed oxygen of the semiconductor crystal. From these facts, it is expected that n-type semiconductors show a large change

in electrical resistance with respect to flammable gas [13]. In fact, it has been reported that the response sensitivity of SnO2 gas sensors is linearly related to the ethanol concentration [14]. In addition, SnO_2 has a higher reaction activity of flammable gas than ZnO, and a semiconductor gas sensor using SnO_2 has the advantages of high sensitivity and high long-term stability. For this reason, SnO_2 has been put to practical use as a material for gas alarms and air quality monitoring sensors. In fact, in 1968, products made from SnO_2 were mass-produced worldwide [15], and the semiconductor gas sensor business started. Semiconductor gas sensor products are broadly divided into household and industrial products, and are now moving toward health and medical care. Table 1.2 shows an application example of the gas sensor. In this way, while the performance of gas sensors using SnO_2 and their application examples are expanding, the correlation between the particle physical properties of oxide semiconductors and sensor characteristics has not been sufficiently studied. One of the physical properties of the particles is the effect of the crystal plane, and if the effect of the crystal plane on the sensor response characteristics is clarified, it is expected that the semiconductor gas sensor can be further improved in performance.

1.2.2. Gas sensing mechanism

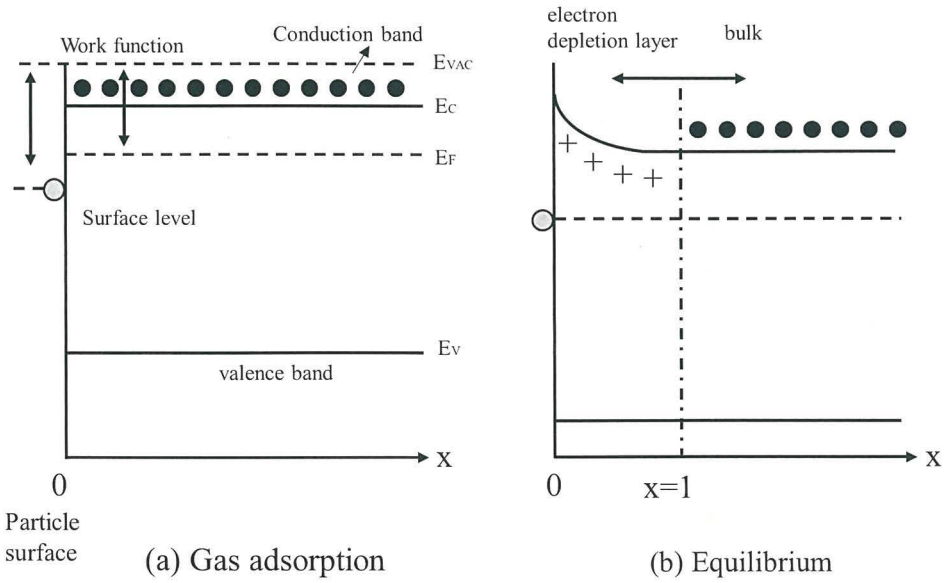

Fig. 1.1 Band model of gas adsorption in n-type semiconductors [16]

The semiconductor gas sensor detects the gas by reading the change in the electrical resistance value in the air and in the test gas. This section describes the detection mechanism of the SnO_2 gas sensor. Here, air is treated as a gas in which 21% O_2 and 79% O_2 are mixed. In addition, N_2 is an inert gas and is not involved in the surface adsorption of SnO_2.

When a gas with a high electron affinity such as O_2 is adsorbed on the surface of SnO_2 particles, those gas molecules are physically adsorbed on the surface of the particles and lose their kinetic energy. The physically adsorbed molecule undergoes thermal dissociation and is chemisorbed on the adsorption site. This will result in a new energy level in which electrons can exist between the Fermi level of the semiconductor and the valence band. When the adsorption reaches an equilibrium state, the Fermi level near the surface of the semiconductor particle and the energy level of the adsorbed molecule match as shown in Fig. 1.1 (b), and electron transfer does not occur. The region with low charge density on the surface represented by the curved line in Fig. 1.1 (b) is called the electron depletion layer.

Next, when a flammable gas is introduced, the gas detection mechanism associated with the adsorption reaction on the SnO_2 surface is shown in the figure.

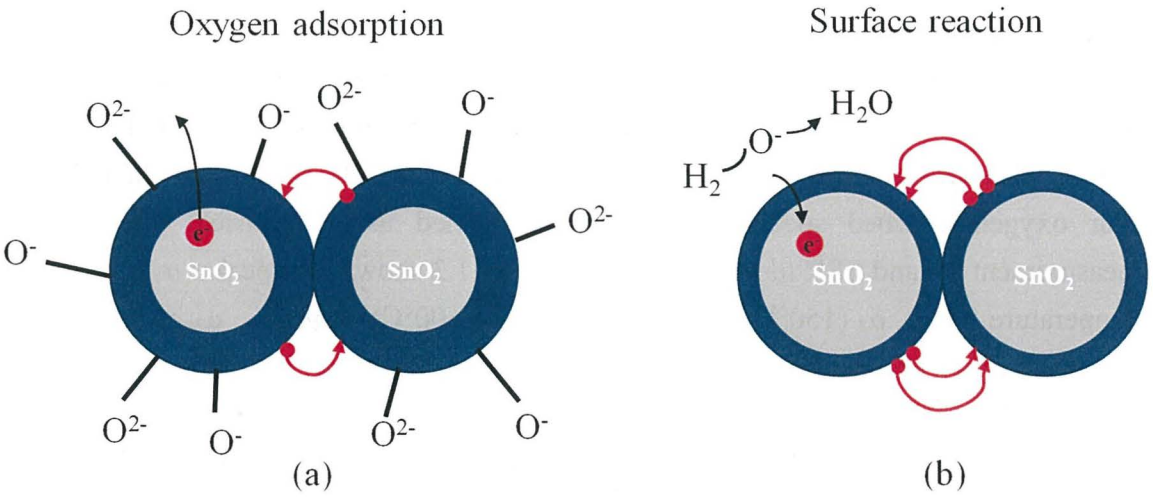

Fig. 1.2 SnO_2 sensor response mechanism (In dry air (a) and In hydrogen mixed air (b))

The oxygen adsorption mechanism in dry air is shown in Fig. 1.2 (a). Oxygen is adsorbed on the particle surface in a negatively charged state and takes electrons from the SnO_2 surface, so the surface charge density of the particle is low and the electrical resistance value is high. This reaction is expressed by the following formula.

$$O_2 + 2e^- = 2O^-_{ad} \quad (1.1)$$

$$O_2 + 4e^- = 2O^{2-}_{ad} \quad (1.2)$$

Next, the surface reaction in the case of hydrogen-mixed air is shown (Fig. 1.2 (b)). This section deals with H_2, which is a typical flammable gas as a test gas. H_2 reacts with adsorbed oxygen (O-or O^{2-}) on the surface of SnO_2 particles in an appropriate temperature range. At this time, the adsorbed oxygen (O-or O^{2-}) is dissociated by this reaction, and the trapped electrons are returned to SnO_2. As a result, the surface charge density increases and the electrical resistance value becomes low. This reaction formula is shown below.

$$H_2 + O^-_{ad}(\text{or } O^{2-}_{ad}) = H_2O + e^-(\text{or } 2e^-) \quad (1.3)$$

The sensor sensitivity is defined as Ra / Rg (Ra: electrical resistance value in air, Rg: electrical resistance value in the test gas), and it can be said that the larger the difference in electrical resistance value, the higher the sensitivity. Therefore, the target gas can be detected by reading the difference in electrical resistance before and after exposure to the test gas.

1.2.3. Oxygen adsorption species on the surface of the device

Figure 1.3 shows the results of temperature desorption measurement (TPD) of SnO_2 to oxygen [17]. It has been confirmed by the thermal desorption measurement (TPD) of O_2 that O_2 is adsorbed on the surface of SnO_2 in the state of O_2, O_2^-, O^-, and O^{2-}. In addition, four oxygen-adsorbed species have been confirmed using electrical conductivity measurement [18] and ESR measurement [19]. Figure 1.3 shows four peaks: α_1 (maximum temperature 80°C), α_2 (150°C), β (520°C), and γ (> 600°C). Peaks α_1, α_2, and β are the peaks obtained by elimination of O_2, and are reported to be O_2, O_2^-, O^-, or O^{2-}, respectively. Of these, O_2 is physical adsorption, and O_2 does not affect changes in electrical resistance. O_2^- is an electron configuration in which one electron enters the antibonding orbital of O_2, and is energetically more stable than O_2 of physical adsorption. O_2^- is easily generated at low temperature if there is an electron donor, but its chemical reactivity is poor. Then, when the temperature is raised to the temperature at which O_2 dissociation occurs, O_2 is adsorbed on the particle surface as O^- or O^{2-} if there is an electron donor. In recent years, these adsorptions have also been obtained by examining the relationship between the

electrical resistance value and the oxygen partial pressure in detail. According to Suematsu et al., Oxygen is competitively adsorbed on the SnO_2 surface in the O^- or O^{2-} state, and their balance and dominant adsorbed species depend on the ambient atmosphere and pretreatment for measurement [20,21]. In addition, the γ peak seen above 600°C is the lattice oxygen of SnO_2, and it is considered that the SnO_2 surface is in a reduced state and the lattice oxygen is released in this region. Among the oxygen adsorbed species, O_2^-, O^-, and O^{2-} affect the electrical characteristics, but O_2^- is desorbed at 250°C or higher, and oxygen that is stably present in the operating temperature range of the actual sensor is only O^- and O^{2-}. This is a tendency obtained from the above-mentioned change in electrical resistance value. Therefore, O^- and O^{2-} are involved in the electrical resistance of SnO_2 and the sensor response.

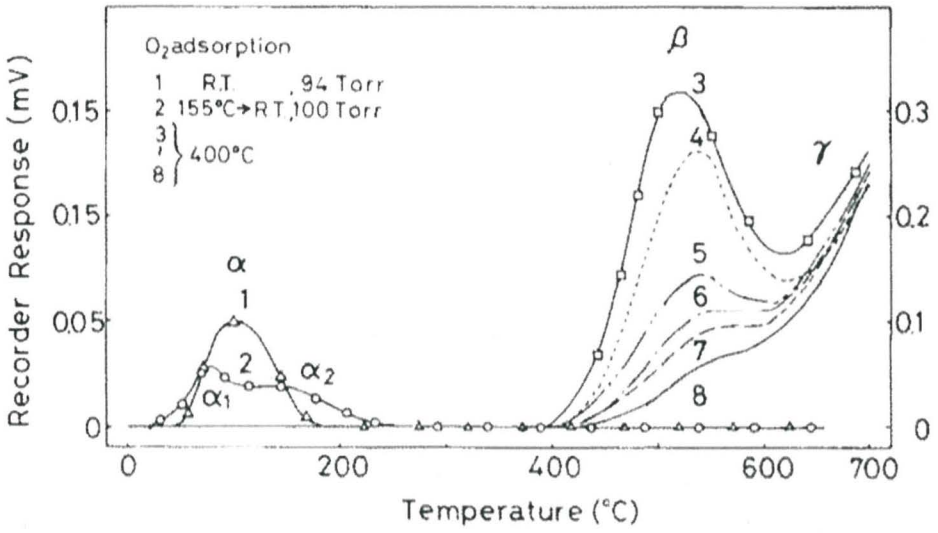

Fig.1.3 The results of temperature desorption measurement (TPD) of SnO_2 to oxygen [17]

The effect of hydrogen adsorption on electrical conductivity has not been confirmed, and it is considered that the sensor response does not need to be considered by hydrogen adsorption. However, it has also been reported that water vapor generated by the surface reaction between hydrogen and adsorbed oxygen is adsorbed on the surface of SnO_2 particles, thereby reducing the electrical resistance value and increasing the sensor sensitivity to H_2. [4].

1.3 Key Factors of Oxide Semiconductor Gas Sensor

Semiconductor gas sensors are used in various gas atmospheres, and it is strictly required to maintain their functions in all atmospheres. Therefore, many studies on receptor function, particle size effect and microstructure control have been conducted to improve the gas detection sensitivity of the sensor. This section describes material design factors for increasing the sensitivity of semiconductor gas sensors.

1.3.1. Receptor function

By dispersing and supporting highly active noble metals and oxides on the particle surface of oxide semiconductors, the sensitivity is improved by a chemical or electronic mechanism. This is a receptor function. The sensitizing effect of the receptor function can be divided into a chemical sensitizing effect and an electronic sensitizing effect. The chemical sensitization effect is a mechanism in which the test gas dissociates and adsorbs on the additive, spills over to the semiconductor surface, and reacts with the adsorbed oxygen there. The other electronic sensitizing effect is provided by a change in the electronic bond between the additive and the metal oxide. As an example, the case where Pd is added will be described. Pd is said to exist as PdO (p-type semiconductor) in the air at the sensor operating temperature, and is said to exist as Pd in a reducing atmosphere (H_2, CO, etc.). That is, in air, PdO and SnO_2 form a p-n junction, at which time PdO significantly reduces the surface charge density of SnO_2 particles as a strong electron acceptor, which increases the electron depletion layer. On the other hand, in a reducing atmosphere, since Pd exists as a noble metal, the p-n junction disappears, the effect as an electron acceptor is lost, and the resistance value decreases more than in air. In addition, the resistance value decreases with the oxidation of the reducing gas. In other words, in the case of Pd support, there are two electronic factors, sensitization due to p-n junction and sensitization due to redox characteristics between PdO-Pd.

In the chemical sensitization effect, the change in electrical resistance value with or without the receptor is small. On the other hand, in the electronic sensitization effect, since the receptor acts as a donor or acceptor, the electrical resistance changes by nearly one frame by supporting the receptor on the surface of the oxide particles. For this reason, the electronic sensitizing action has attracted much attention. In addition, supporting platinum on a ZnO sensor increases the sensitivity of isobutane and propane,

while supporting palladium increases the detection sensitivity of H_2 and CO [22]. From this, it is suggested that the effect of the receptor function not only increases the sensitivity of the sensor but also significantly affects the gas selectivity

1.3.2. Transducer function

In the oxide, the fine particles are physically in contact with each other at the grain

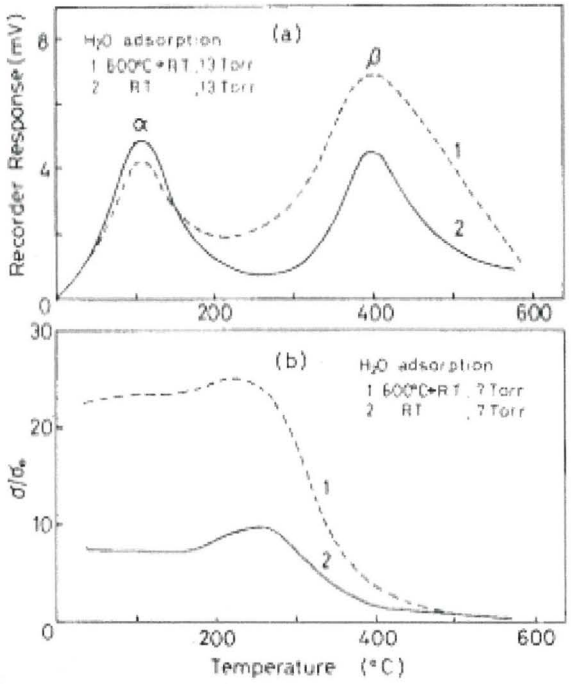

Figure 1.4 Crystalline dependence of SnO_2 element electrical resistance and sensor sensitivity [24]

boundaries or are connected by a neck portion smaller than the particle size. The electrical resistance value of a semiconductor gas sensor is said to be dominated by the resistance at the grain boundaries or neck. Xu et al. Reported the effect of crystallite diameter (D) on gas sensitivity [23]. In Figure 1.4 The dependence between the electrical resistance value and the crystallite diameter of the sensor sensitivity is shown. When the crystallite diameter is reduced, the electrical resistance value (Ra) in the air is constant up to twice the Debye length (L) (2L), and the dependence on the particle size does not appear. When the crystallite diameter becomes smaller than 2L, the electric resistance value increases sharply. This phenomenon is also observed for the electrical resistance value (Rg) in 800ppm H_2, and as a result, it shows an increase in gas sensitivity (Ra / Rg) when the crystallite diameter is 2L or less.

From the report of Ogawa et al., In the case of SnO_2, the Debye length is estimated to be about 3 nm at 300 °C [25]. From this, 2L is considered to be about 6 nm, which is in good agreement with the results in the figure. Komen et al. Argue that in the region where D (grain size) >> 2L, the resistance at the grain boundary contact part and the neck part becomes high, and the resistance between the grain boundary and the neck part determines the resistance value of the device. On the other hand, in the region where D << 2L, the electron depletion layer spreads over the entire particle, and the resistance of the crystallite itself is overwhelmingly dominant over the grain boundary (crystallite control) [26]. Therefore, the resistance value of the device in the crystallite diameter control region rapidly increases in the air and the test gas, resulting in an increase in gas sensitivity. From this, it was suggested that the control of the crystallite diameter of the sensor is important for improving the gas sensitivity.

The above interpretation is based on the premise that electron conduction is performed by the Schottky model (Fig. 1.5 (a)). On the other hand, Yamazoe et al. Report that electron transport may occur due to the tunnel effect when the interparticle distance is small (Fig. 1.5 (b)). The occurrence of tunnel conduction means that there is an electric charge on the particle surface. Therefore, a theoretical interpretation was made on the adsorption and reaction of the electric charge and gas existing on the surface [28].

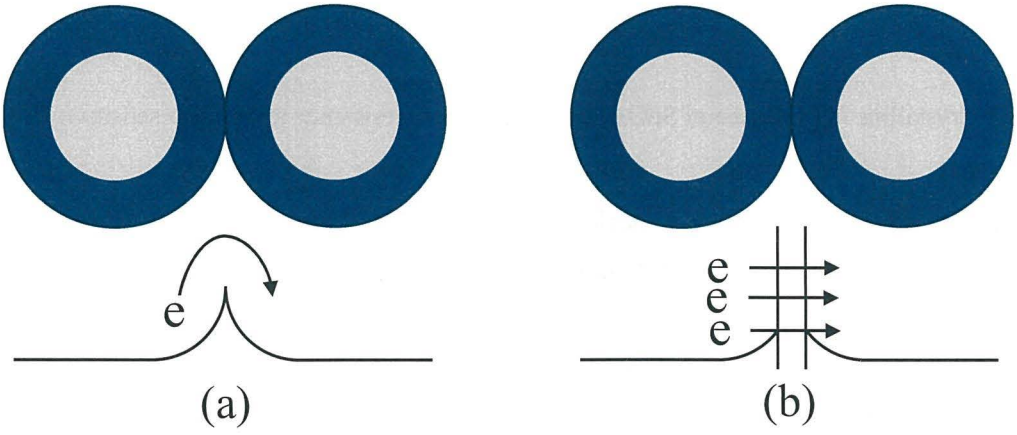

Fig. 1.5 Electrical conduction models [27]

(a) Schottky model (b) Tunnel conduction model

It is generally known that the electric resistance value (R) of a semiconductor gas sensor depends on the partial pressure (P) of the test gas, and the resistance value can be expressed by the following equation.

$$R=A\cdot P^{\alpha} \text{ or } \log R = A' + \alpha \cdot \log P \qquad (1.4)$$

Here, A, A', and α are constants, and the power index α is peculiar to the type of the test gas. In the case of SnO_2, α is 1/2 for surface O_2 adsorption and α is -1 / 2 for surface H_2 adsorption.

Figure 1.6 shows the change in surface potential when the crystallite diameter is reduced when the oxygen partial pressure is changed with respect to the particles. When the oxygen partial pressure (PO_2) is 0, it is in a flat band state regardless of the crystallite diameter. First, when SnO_2 having a large crystallite diameter introduces a small amount of O_2 and becomes PO_2 (I) under low oxygen partial pressure, the surface charge density decreases with the adsorption of oxygen, and an electron depletion layer is formed from the particle surface to the inside. Here, when the oxygen partial pressure is increased, the depletion layer spreads inside the crystallite as the amount of negative charge adsorption of O_2 increases, and it spreads over the entire crystal at a certain oxygen partial pressure PO_2 (II). Become. It was said that this was a particle size effect based on the Schottky model (the electrical resistance value and sensor sensitivity increased sharply from this state). When the oxygen partial pressure is further increased, negative charge adsorption of oxygen occurs. At

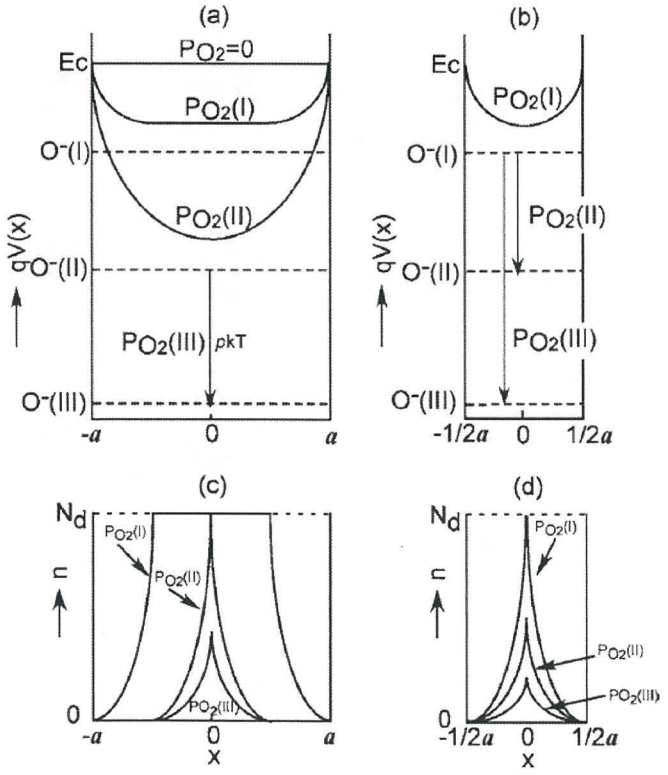

Figure 1.6 Surface potential effect of semiconductor particles on oxygen partial pressure[16]
(a): Crystallet diameter 2a, (b): Crystallet diameter a

this time, it is said that the source of electrons is inside the crystal, and after the depletion layer spreads throughout the crystal, the electrons are supplied by lowering the Fermi level.

Figure 1.7 shows the spreading state of the depletion layer using a spherical particle model. Here, the oxygen partial pressures PO_2 (I) to (III) and the crystallite diameter 2a correspond to those in Fig. 1.7. From the figure, the situation in which the electron depletion layer spreads from the crystal surface to the inside is defined as Regional depletion (PO_2 (I)). After that, the depletion state (PO_2 (II)) when the depletion layer spread over the entire crystal was defined as Boundary depletion, and the depletion state (PO_2 (III)) obtained by lowering the Fermi level was defined as Volume depletion. It is said that such a change in the depletion state is caused by a change in the crystallite diameter and donor density of the semiconductor, and that the depletion state of the semiconductor shifts from the regional depletion to the volume depletion as the crystallite diameter and donor density decrease.

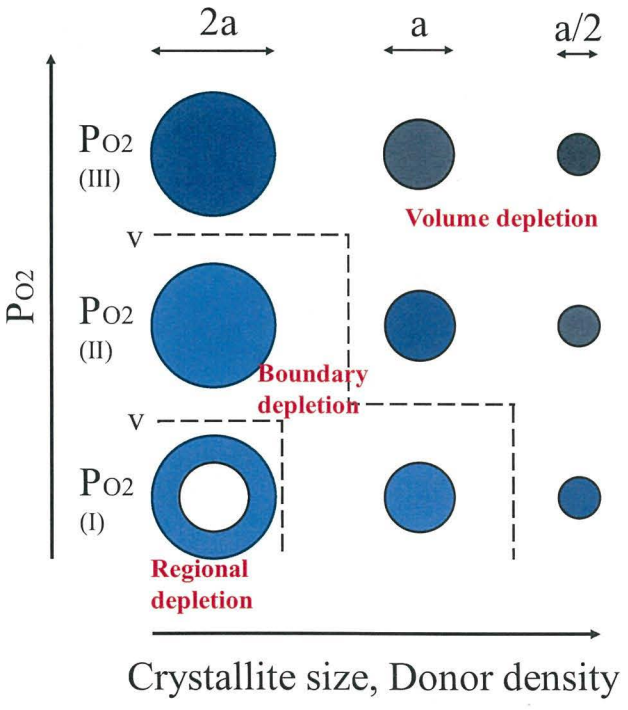

Figure 1.7 Depletion state change of spherical particles

Theoretical analysis has also been performed on the sensitivity to hydrogen, and the sensor sensitivity (Ra / Rg) in the depletion state of Volume depletion obtained by lowering the Fermi level is expressed as follows [29].

$$\frac{R_a}{R_g} = \{1 + \left(\frac{3c}{aN_D} \right) \cdot P_{H2}\}^{\frac{1}{2}} \qquad (1.5)$$

$$\left(\frac{R_a}{R_g} \right)^2 = 1 + \left(\frac{3c}{aN_D} \right) \cdot P_{H2} \qquad (1.6)$$

From this, it can be seen that the square of the sensor sensitivity is proportional to the partial pressure of hydrogen, and is also proportional to the reciprocal of the crystallite diameter and donor density.

In this way, the relationship between the depletion theory of semiconductors and the surface interaction of gas is interpreted by the development of the relationship between particle size and donor density. It is considered that not only the semiconductor itself but also the electron trap on the particle surface accompanying the support of the receptor can be developed. It is considered that the formation of the pn junction by carrying the receptor shows an effect similar to the decrease in donor density, and enables the transition to Volume depletion under hypoxic partial pressure.

1.3.3. Utility factor

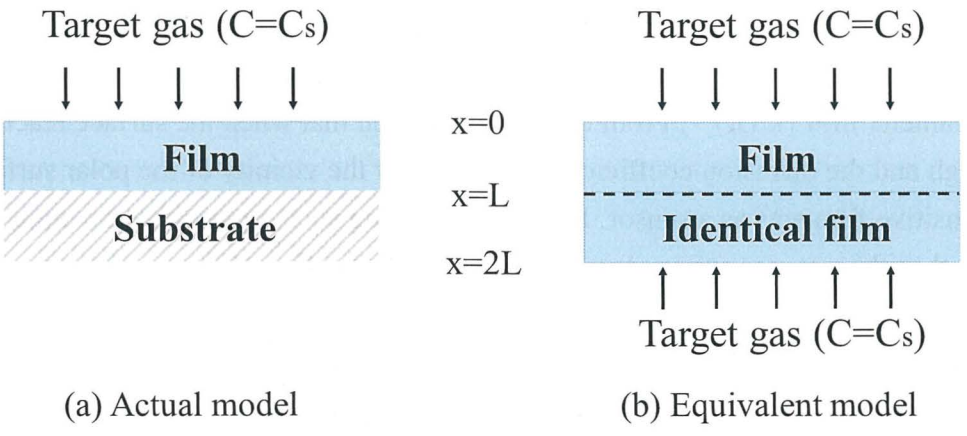

Figure 1.8 Diffusion model of thin film sensor

The gas diffusion mechanism in a porous material, such as a semiconductor gas sensor element, depends on the pore size. SnO_2 is difficult to sinter and crystal growth is suppressed. From this, it is considered that the gas diffusion in the pores in the sensitive membrane is the diffusion (Knusen diffusion) in which the collision between molecules can be ignored and is controlled only by the collision between the sensitive membrane and the gas molecule. Figure 1.8 shows a gas diffusion model of the sensor, assuming a porous thin film on an alumina substrate.

Assuming that C = Cs when x = 0 and dC / dx = 0 when x = L as the boundary conditions for gas diffusion, the film thickness dependence of the gas sensitivity of the thin film solves the gas reaction-diffusion equation in the porous layer. By doing so, it can be expressed as follows. (k: reaction rate constant, Dk: Knudsen diffusion coefficient)

$$C=C_s \cdot \frac{\cosh\{(L-x)\cdot(k/D_k)^{1/2}\}}{\mathrm{coh}\{L\cdot(k/D_k)^{1/2}\}} \qquad (1.7)$$

From this equation, the gas concentration C is governed by the k / Dk value. The greater the diffusion distance from the surface, the lower the gas concentration. The smaller the diffusion rate of gas and the larger the reaction rate constant, the lower the gas concentration inside. When the k / Dk value is small, the test gas diffuses over the entire sensor membrane, and the entire sensor membrane functions as a sensor. On the other hand, when the k / Dk value is large, it stays near the film surface, and only the vicinity of the sensitive film surface acts as a sensor. Fig.1.9 assumes that the reaction rate is proportional to the gas concentration (C) (rate constant k), and shows how the gas concentration decreases in the depth direction (x) in the sensitive film in the steady state. Parameter $m=L(k/D_k)^{1/2}$. From this, it can be seen that when the surface reaction rate is high and the diffusion coefficient is small, only the vicinity of the polar surface of the sensitive film acts as a sensor. Examination using such a gas diffusion equation revealed that the gas sensitivity largely depends on the film thickness [57], the gas diffusion coefficient, and the reaction rate constant.

It has been reported that 1 ppb level of toluene can be detected by fusing the above three functions [30]. However, research on gas detection selectivity is still inadequate. Here, it is considered that the crystal plane control can improve the sensor sensitivity and selectivity. Section 1.4 describes the effect of crystal planes on gas sensors.

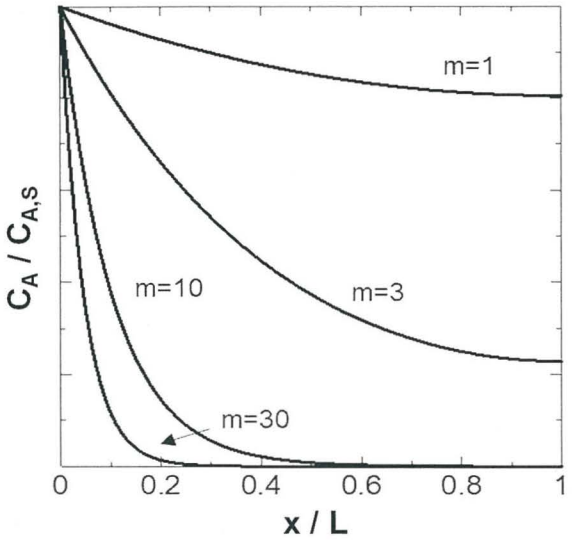

Figure 1.9 Change in gas concentration with respect to film thickness

1.4. Reaction site

1.4.1. Introduction

In the conventional research, in order to improve the gas detection sensitivity of the gas sensor, the research has been carried out focusing on the receptor function [31)-(34)], the particle size/shape effect[35)(36)(53)] and the microstructure control[37)(38)]. In these studies, it has become clear that the sensor sensitivity of a semiconductor gas sensor is determined by the properties of the crystal surface in direct contact with the test gas.

The metal oxide used in the semiconductor gas sensor has a crystal structure peculiar to each oxide, and the exposed elements and their coordination numbers differ depending on the crystal plane. Therefore, it has been reported that the surface energy differs depending on the exposed crystal plane, and the oxygen adsorption state, adsorption amount, and reactivity differ [39)]. At the same time, some research also has shown that the sensor characteristics may be related to the exposed crystal planes [40)]. From this, it is considered that the gas sensor, which also emphasizes the surface state of the material, is affected by the crystal plane of sensitivity. The effect of the crystal plane will be explained in the next section.

1.4.2. Function of exposed crystal faces

In recent years, research on the effect of exposed crystal planes of metal oxides such as SnO_2 and ZnO on sensor sensitivity has begun. The summary is shown in the Table 1.3.

Table 1.3 A list of research on the effect of exposed crystal planes of metal oxides

Author	Sensor materials	Sensor response	Crystal face	Detected gas	literature
Kim et al	SnO_2 (films)	50-100 (400 °C,1000 ppm)	(101)	Ethanol	Sensors and Actuators B 147 (2010) 653–659[41]
Kim et al	SnO_2 (films)	1-10 (500 °C,1000 ppm)	(001)	Ammonia	Sensors and Actuators B 147 (2010) 653–659
Kim et al	SnO_2 (films)	380 (400 °C,1000 ppm)	(001)	Hydrogen	Sensors and Actuators B 147 (2010) 653–659
Yusuf V et al	ZnO (nanoplates)	24.6 (300 °C,100 ppm)	(0001)	Ethanol	Phys. Chem. Chem. Phys., 2014, 16, 11471[42]
Xu et al	ZnO (nanosheets)	~80 (330 °C,50 ppm)	(0001)	Ethanol	Sensors and Actuators B 242(2017)148-157[43]
Ahmed.A et al	SnO_2 (nanostructured thin films)	-	(110)	Ethanol Acetone	J. Mater. Chem. A, 2018, 6, 2053[39]
Saito et al	ZnO (pyramid-shaped particles)	10000 (50 ppm)	(0001)	Ethanol	J. Phys. Chem. C 2018, 122, 13, 7353–7360[44]
Xu et al	SnO_2 (nanosheets)	207 (200 °C,200 ppm)	(001)	Formaldehyde	Sensors and Actuators B 289(2019)186-194[45]
Zhang et al	Au-SnO_2	77.5 (183 °C,100 ppm)	(221)	Acetylene	Sensors and Actuators B 307(2020)127629[46]

In the case of ZnO, which is one of the materials used for semiconductor gas sensors, the adsorption of ethanol on the (0001), (1010) and (1120) planes of ZnO was simulated by DFT (density functional theory). It was found that the (0001) plane of the ZnO nanoplate promotes ethanol adsorption by interacting with the surface oxygen p orbital, and at the same time, it extends the OH bond and lowers the adsorption energy to increase the sensitivity of the ZnO nanoplate. From Xu et al. [43], the (0001) and $(10\bar{1}0)$ planes of ZnO also show the atomic model. Zn and O of hexagonal ZnO are known to be tetra-coordinated and are usually unsaturated on the surface. As shown in the figure, on the (0001) plane, the Zn atoms are 2-coordinated or 3-coordinated, and all are unsaturated. However, on the$(10\bar{1}0)$ side, most Zn are 4-coordinated sites and the remaining few are 3-coordinated sites. From this, it can be seen that the (0001) plane has more oxygen vacancies than$(10\bar{1}0)$and can react more actively with the electrons from the conduction band. It was also calculated that the reduction energy when oxygen molecules were adsorbed on the (0001) plane was 1.0665 eV, and that on the plane was 0.5233 eV. The higher the reduction energy, the stronger the chemical adsorption of oxygen, indicating that the (0001) plane can be more easily adsorbed than$(10\bar{1}0)$. Moreover, since the sensor sensitivity of the (0001) plane is clearly higher than that of the $(10\bar{1}0)$ plane regardless of the concentration of ethanol [43], the sensor sensitivity of ZnO strongly depends on the exposed crystal plane, and the (0001) plane is used. It can be seen that the sensor performance can be improved by exposing it.

As described above, the sensor characteristics of ZnO differ depending on the crystal plane, but the relationship between the crystal plane of SnO_2 nanoparticles, which are also metal oxides, and the sensor response characteristics has not yet been

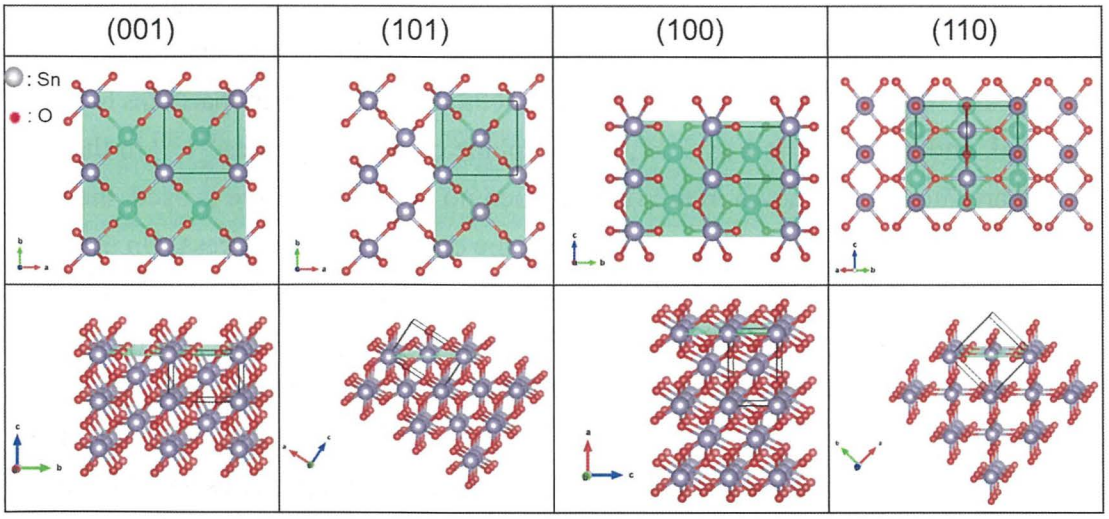

Figure 1.10 Schematic diagram of each crystal plane

clarified. SnO_2 has a rutile type, and a schematic view of planes (001), (101), (100) and (110) viewed from above and from the side is shown in Fig. 1.10. In this way, it has been reported that the positional relationship between Sn and O differs depending on the crystal plane, and that the surface energy (Binding energy of Sn and O) is in the order of (110) <(100) <(101) <(001) [47]. From this, it can be seen that the adsorption state, adsorption amount and reactivity of the gas on the SnO_2 surface are different. Therefore, in a gas sensor that converts a surface reaction into an electric signal, it is considered that the crystal plane affects the sensor characteristics and gas selectivity as in ZnO.

In recent years, S.-H. Hong et al. have produced epitaxially grown SnO_2 thin films with exposed (100), (001), (110) and (101) by the PLD method for gas sensors using SnO_2, and sensor response characteristics to various gases. The result of the evaluation was reported [48]. As a result, the sensor response characteristics to ethanol tended to be highest on the (101) plane and lowest on the (110) plane. On the other hand, for ammonia, the (001) plane showed high sensor sensitivity. In this way, although it has been reported by model experiments that the crystal plane of SnO_2 contributes to the sensor sensitivity, the exposed crystal plane and sensor response characteristics of the particulate SnO_2 gas sensor reflect the transducer effect and microstructure. No correlation with is obtained. In order to evaluate these correlations using particulate SnO_2, it is indispensable to develop SnO_2 nanoparticles that control the exposed crystal plane and suppress other effects.

1.4.3. Method for controlling the exposed crystal faces

In order to clarify the sensor response characteristics to the crystal plane, it is indispensable to synthesize particles having a controlled exposed crystal plane. In recent years, research on crystal plane control methods for oxide nanoparticles has been advanced, and as shown in Fig. 1.11, crystal plane control examples [49,50] in the case of ceria are shown. As shown in the figure, when no organic additive is used, the most stable surface of CeO_2 (111) is exposed during the crystal growth process. On the other hand, when an organic additive is added, the organic additive is adsorbed on the surface (100), which is the most unstable surface (the surface energy is large), and the surface energy is lowered. Therefore, the growth of the (110) plane is suppressed, and finally the most unstable (100) plane is exposed CeO_2. At this time, if the amount of the organic additive added is too large, it is adsorbed on the entire particles and it becomes difficult to control the crystal plane. By modifying a specific surface of the particle surface with an organic additive in this way, the crystal plane can be selectively

exposed, and optimization of the amount of the organic additive added is important for optimizing the exposed crystal plane.

In the case of SnO_2, by using amine-based additives such as ethylenediamine (EDA) [51], triethanolamine [51] and tetramethylammonium aqueous solution (TMAH) [52], the exposed crystal planes of SnO_2 nanoparticles can be used. It has been reported that crystal growth can be controlled. Therefore, in this study, we attempted to control the crystal plane of SnO_2 using additives.

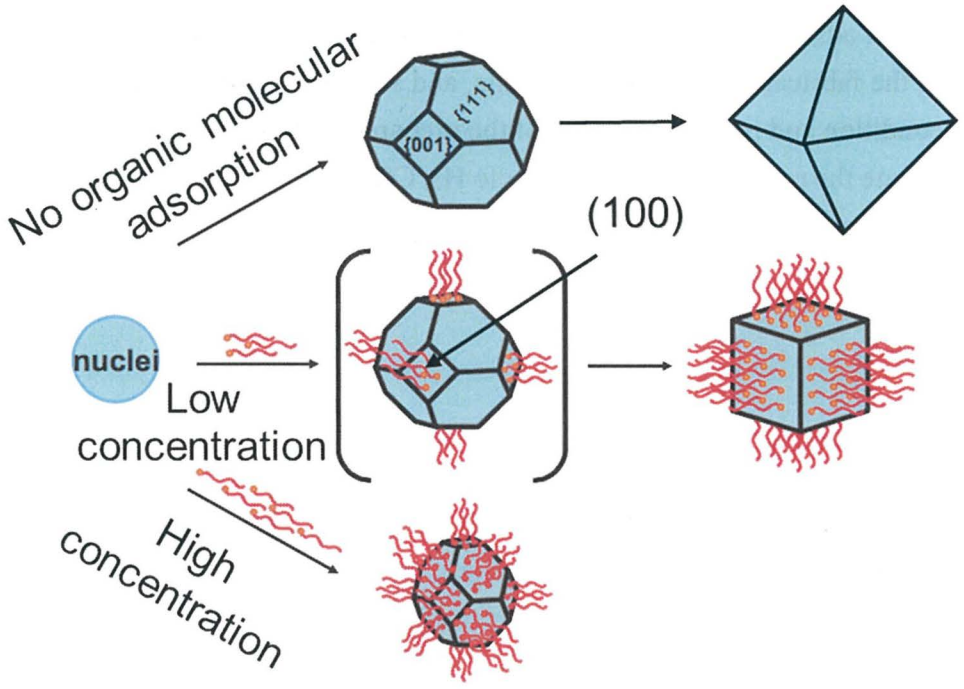

Figure 1.11 Crystal plane control of ceria

1.5. Motivation

As in the previous section, from the binding energy of Sn and O ((110) <(100) <(101) <(001) [47]), it is considered that reactivity of the gas on the SnO_2 surface are different. In addition, crystal face of SnO_2 is also reported recently to relate to the Binding energy with Ethanol[39]. Therefore, it is considered that the crystal plane of SnO_2 affects the sensor characteristics such as sensor sensitivity and selectivity as well as ZnO. There have been many reports on the improvement of gas sensor sensitivity by the crystal plane of SnO_2. However, research on the selectivity of gas sensors and high-sensitivity detection of gas is still insufficient.

Therefore, the purpose of this study is to clarify the relationship between sensor response characteristics and crystal planes. At the same time, some research also has shown that the particles' characteristics may be related to the calcination temperature [54]. Therefore, the effect of the calcination temperature of SnO_2 on anisotropic growth and gas sensor response was also investigated. Focusing on TMAH and 1,6-diaminohexane as amine-based additives, we will investigate the effects on crystal growth and the sensor characteristics of synthesized anisotropic nanoparticles. At that time, the sensitivity to H_2 and CO is investigated to detect the surface acidity of tin oxide. In addition, the sensitivity to ethanol with different reaction pathways will be measured to investigate the effect of the number of adsorbed oxygen consumed. Chapter 2 describes the preparation of sensor materials, the fabrication of sensor elements, and sensor measurement. In Chapter 3, the surface condition and pore distribution of the prepared material are evaluated. In Chapter 4, we evaluate the responsiveness of SnO_2 to H_2, CO, and ethanol. Chapter 5 summarizes this paper and concludes with an acknowledgment.

Chapter 2.

Preparation

2.1. Introduction

In order to prepare anisotropic SnO_2, controlling the conditions of hydrothermal treatment is an effective way. The research of our laboratory has come up with the conjecture that additives can effectively control the growth of anisotropic particles. In this chapter, SnO_2 were synthesized by using the hydrothermal treatment, sensor devices were manufactured and measured using the obtained SnO_2.

2.2. Synthesis of SnO_2 solution by using the hydrothermal treatment

In this study, SnO_2 was prepared using a hydrothermal synthesis method. A list of chemicals used in the experiment is shown in table 2.1, the flowchart of SnO_2 preparation by hydrothermal treatment is shown in Figure 2.1. The preparation method used in this study is based on the liquid phase method, which makes it easy to control the particle size and shape, control the components and composition, and relatively easily control the dispersibility and cohesiveness of the produced fine particles. 1M of aqueous solution was respectively prepared using Tin(IV) Chloride Pentahydrate ($SnCl_4.5H_2O$) and ammonium bicarbonate (NH_4HCO_3) as starting materials. 2M of ammonium nitrate (NH_4NO_3) was prepared as a coprecipitant.

A white tin acid precipitate was obtained by placing the $SnCl_4$ aqueous solution in a burette and dropping it into the NH_4HCO_3 aqueous solution. The $SnCl_4$ aqueous solution and the NH_4HCO_3 aqueous solution were mixed so as to have a volume ratio of 1: 5. After the dropping, the mixture was stirred for 1.5 hours to allow a sufficient reaction, and then the stirring was stopped and the mixture was allowed to stand overnight. Cl^- was removed by washing the obtained white precipitate for 10 times (stannic acid gel) (centrifugation: 3000 g, 10 min, 10°C). At the time of washing (Cl^- removal), 50 ml of an aqueous ammonium nitrate solution (2 M) was added as a coprecipitant. After the 10th washing was completed, silver nitrate ($AgNO_3$) was added dropwise to the supernatant, and the presence or absence of white precipitate (AgCl) was confirmed to evaluate the

presence or absence of Cl- residue. Then, the stannic acid gel was washed twice

Table 2.1 A list of chemicals used in this experiment

Chemicals	Chemical formula	Purity / %	Chemical company
Tin chloride penta-hydrate	$SnCl_4 \cdot 5H_2O$	98	Fujifilm Wako Pure Chemical Corporation
Ammonium bicarbonate	NH_4HCO_3	20 - 23(as NH3)	Fujifilm Wako Pure Chemical Corporation
Ammonium nitrate	NH_4NO_3	98	Fujifilm Wako Pure Chemical Corporation
Tetramethylammonium (TMAH)	$(CH_3)_4NOH$	15	Fujifilm Wako Pure Chemical Corporation
Ethylenediamine (EDA)	$C_3H_{10}N_2$	98	TOKYO CHEMICAL INDUSTRY
Hexanediamine (HDA)	$C_6H_{16}N_2$	99	TOKYO CHEMICAL INDUSTRY
Ammonia Solution	NH_3	28	Fujifilm Wako Pure Chemical Corporation
Hydrogen peroxide	H_2O_2	30	Fujifilm Wako Pure Chemical Corporation
α-terpineol	$C_{10}H_{18}O$	98	Fujifilm Wako Pure Chemical Corporation

(centrifugation: 12000 g, 10 min, 10°C.) to remove residual ammonium nitrate. An appropriate amount of purified water is mixed with the obtained tinate gel, the pH is adjusted with a tetramethylammonium hydroxide solution (TMAH), and then the mixture is transferred to a carbon-containing PTFE container (manufactured by San-ai Kagaku Co., Ltd.) for hydrothermal treatment was performed using a container (manufactured by San-ai Kagaku Co., Ltd.). When adjusting the pH to 13.7, it was adjusted using a polypropylene beaker (manufactured by Tokusige Chemicals Co., Ltd.). The high temperature reaction vessel was transferred to a constant temperature dryer (DRN320DD model, manufactured by ADVANTEC) and subjected to hydrothermal treatment. Here, the high-temperature reaction vessel was allowed to stand in the center of the constant temperature dryer and subjected to hydrothermal treatment. The obtained SnO_2 nanoparticle dispersion sol was dried at 120°C overnight to obtain a SnO_2 dry powder.

This powder was crushed in an agate mortar and calcined in oxygen for 3 hours using a tube furnace to obtain SnO_2 calcined powder.

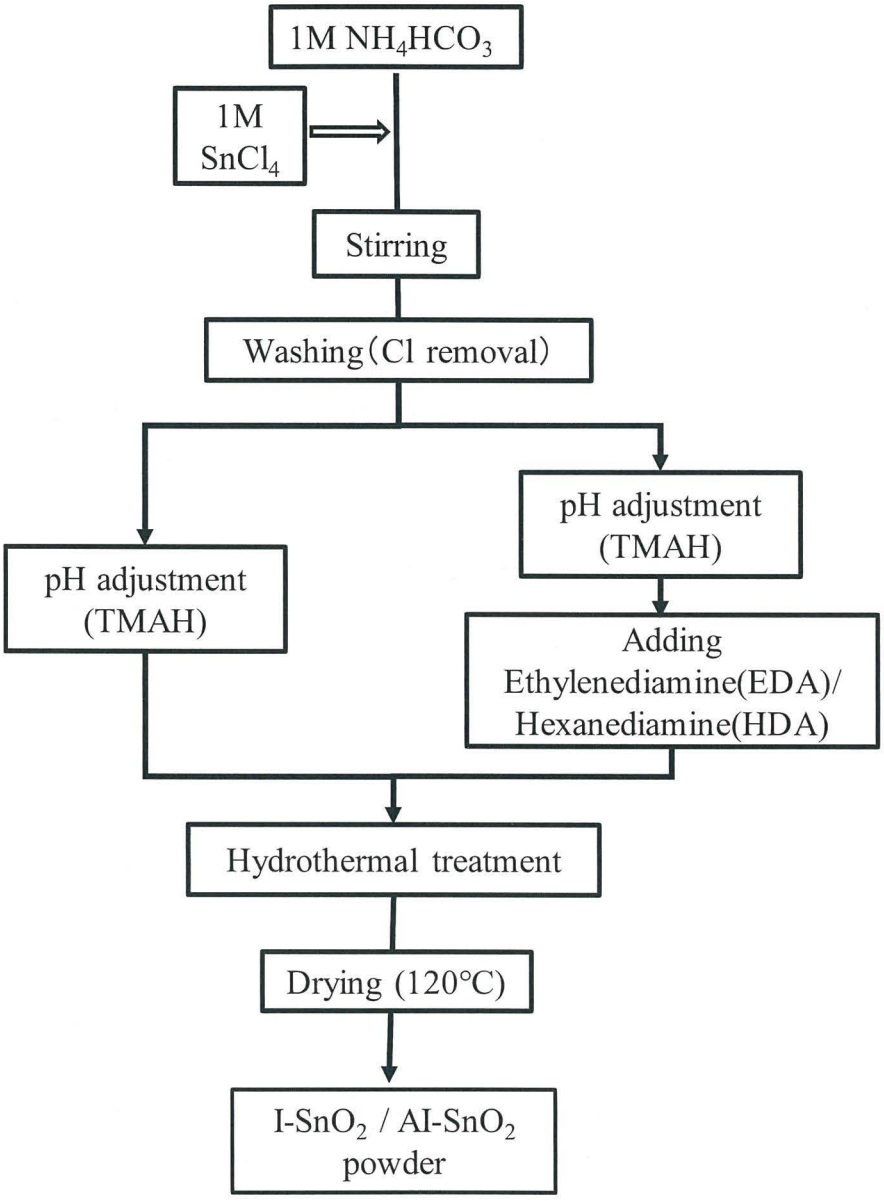

Fig 2.1 The flowchart of SnO_2 preparation

2.3. Material evaluation

2.3.1. X-ray diffraction (XRD) method and fundamental parameter (FP) method

Compounds were identified for the prepared samples by X-ray diffraction. A desktop X-ray diffractometer (Rigaku Co., Ltd., Mini Flex) was used for the X-ray diffraction measurement. The measurement conditions were CuKα (40 kV, 30 mA) for the X-ray source, 2.0°/ min for the scan speed, 0.02 ° for the scan step, and 2θ = 20 ° to 80 ° for the scan range. In addition, compounds were identified for the obtained XRD patterns.

In the FP method, the x-ray intensity of each analytical element is theoretically calculated from the physical constants such as the spectral distribution of the primary x-ray from the x-ray tube, the mass absorption coefficient, and the fluorescence yield, and the composition of the sample is calculated by the sequential approximation method. Is calculated. Therefore, in principle, any combination of elements can be analyzed as long as the sensitivity constant of each element unique to the analyzer is obtained.

2.3.2. Observation by Transmission Electron Microscope (TEM)

The prepared SnO_2 powder was taken and diluted with ethanol to 0.1 wt%. A carbon mesh was sandwiched between tweezers, then soaked in this solution, dried in vacuum for one day, and then the sample was observed using a transmission electron microscope (Hitachi H-7650).

2.3.3. Observation by Field Emission Scanning Electronic Microscopy (FE-SEM)

In order to finely observe the surface structure of the prepared SnO_2 powder, observation was performed with a scanning electron microscope.

A carbon tape was attached to the SEM observation holder, and a small amount of powder sample was taken using a spatula and placed on the holder. This was placed in a Scanning Electronic Microscopy (JSM-6701FMW) and observed.

2.3.4. Specific surface area and pore distribution by BET method

In this study, the measurement was performed using an automatic specific surface area / pore distribution measuring device (BELSORP-mini II, manufactured by Nippon Bell Co., Ltd.). First, an appropriate amount of SnO_2 powder was placed in a sample tube and pretreated. In order to remove the adsorbent on the sample surface, a vacuum heat treatment was performed in the sample tube. After that, the accurate weight of the sample

was measured, the sample was kept at a constant temperature, and the changes in pressure and adsorption amount were measured.

2.3.5 Observation of sensor element film thickness with a laser microscope

A shape analysis laser microscope (KEYENCE, VK-X1000) was used to observe the manufactured sensor element at a magnification of 400 times to evaluate the film thickness of the sensor film.

2.4. Preparation of sensor experimental device

2.4.1. Preparation of device

First, a comb-shaped gold electrode was prepared on an alumina substrate. A commercially available alumina substrate (13 x 9 x 0.5 mm Fine Ceramics Co., Ltd.) was washed with acetone, and a comb-shaped metal electrode (distance between electrodes 90 μm) was printed using a screen printing machine (MITANI ELECTRONICS, MEC-2400). This was calcined in a box-type electric furnace (S-70, manufactured by Denken Co., Ltd.) at 850 ° C for 3 hours to obtain an alumina substrate with a comb-shaped gold electrode (Fig 2.4(a)). Prior to application of the sensor material, the substrate was washed with a mixed solution of H_2O_2, aqueous ammonia and purified water to remove organic impurities on the surface of the alumina substrate.

α-Terpineol was added as a binder to SnO_2 powder to make a paste. This paste was

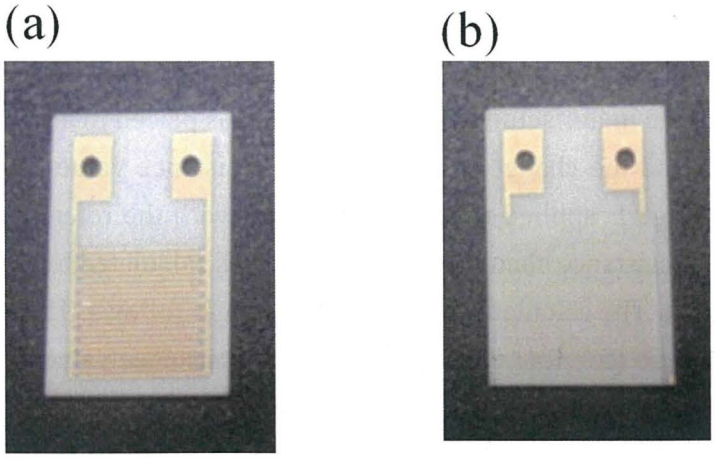

Fig 2.2 Photograph of sensor element

(a) comb-shaped gold electrode

(b) sensor device with SnO_2 paste

applied to an alumina substrate with a gold electrode and dried at 120°C for 1 hour. After that, it was wound around two holes of the alumina substrate using a platinum wire, and gold paste was further applied to the contact portion between the sensor substrate and the platinum wire to form a sensor device (Fig 2.2(b)). Figure 2.3 shows a schematic diagram of the sensor device.

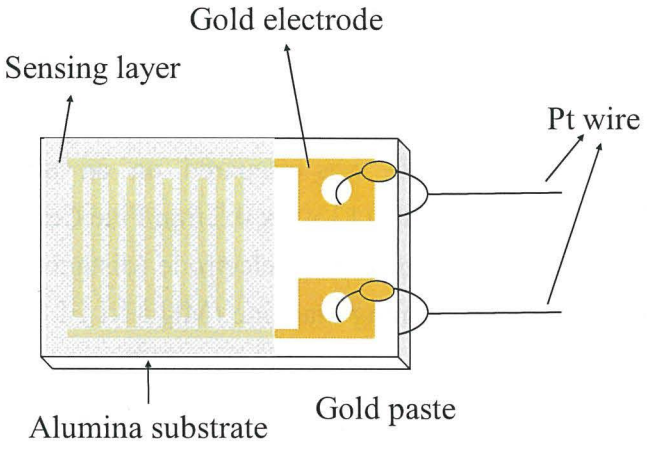

Fig2.3 A schematic diagram of the sensor device

2.4.2. Preparation of measuring device

Figure 2.4 shows the electric circuit for measuring the electrical resistance of the sensor element. Figure 2.5 shows a schematic diagram of the electrical resistance value measuring device. The manufactured sensor element was placed in a sample holder in the measurement cell, and the change in the electrical resistance value of the element was measured. The voltage E applied to the series circuit with the reference resistance was fixed at 4V, and the resistance change of the element was calculated by the voltage change of the sensor element. The calculation formula is shown as follows. The sensor sensitivity was defined as the ratio (S = Ra / Rg) of the electrical resistance value (Ra) in Air and the electrical resistance value (Rg) in the target gas coexisting Air.

$$R = r \cdot (E/V - 1) \qquad (2.1)$$

V: Output voltage

E: Applied voltage

r: Reference resistance

R: Element resistance

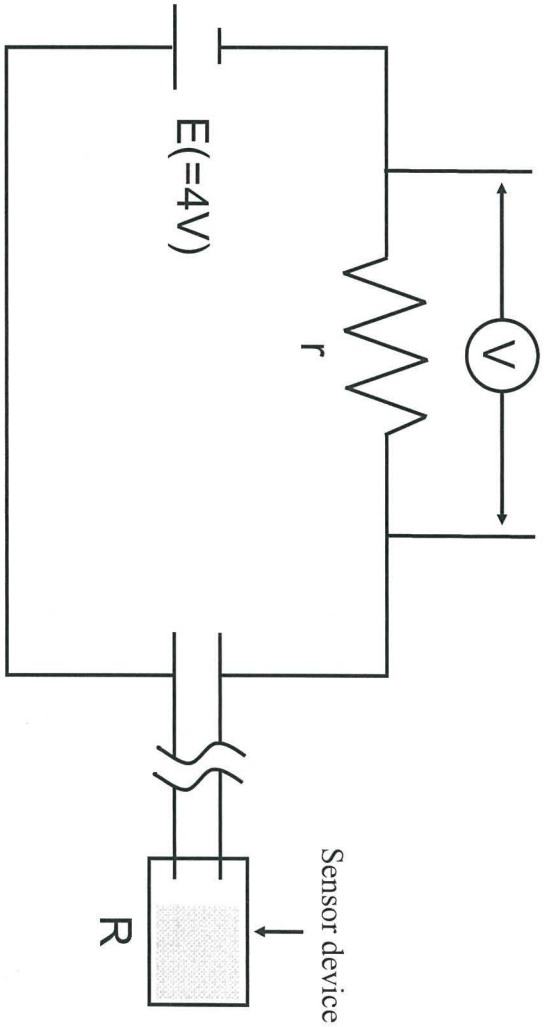

Fig 2.4 the electric circuit for measuring the electrical resistance of the sensor element

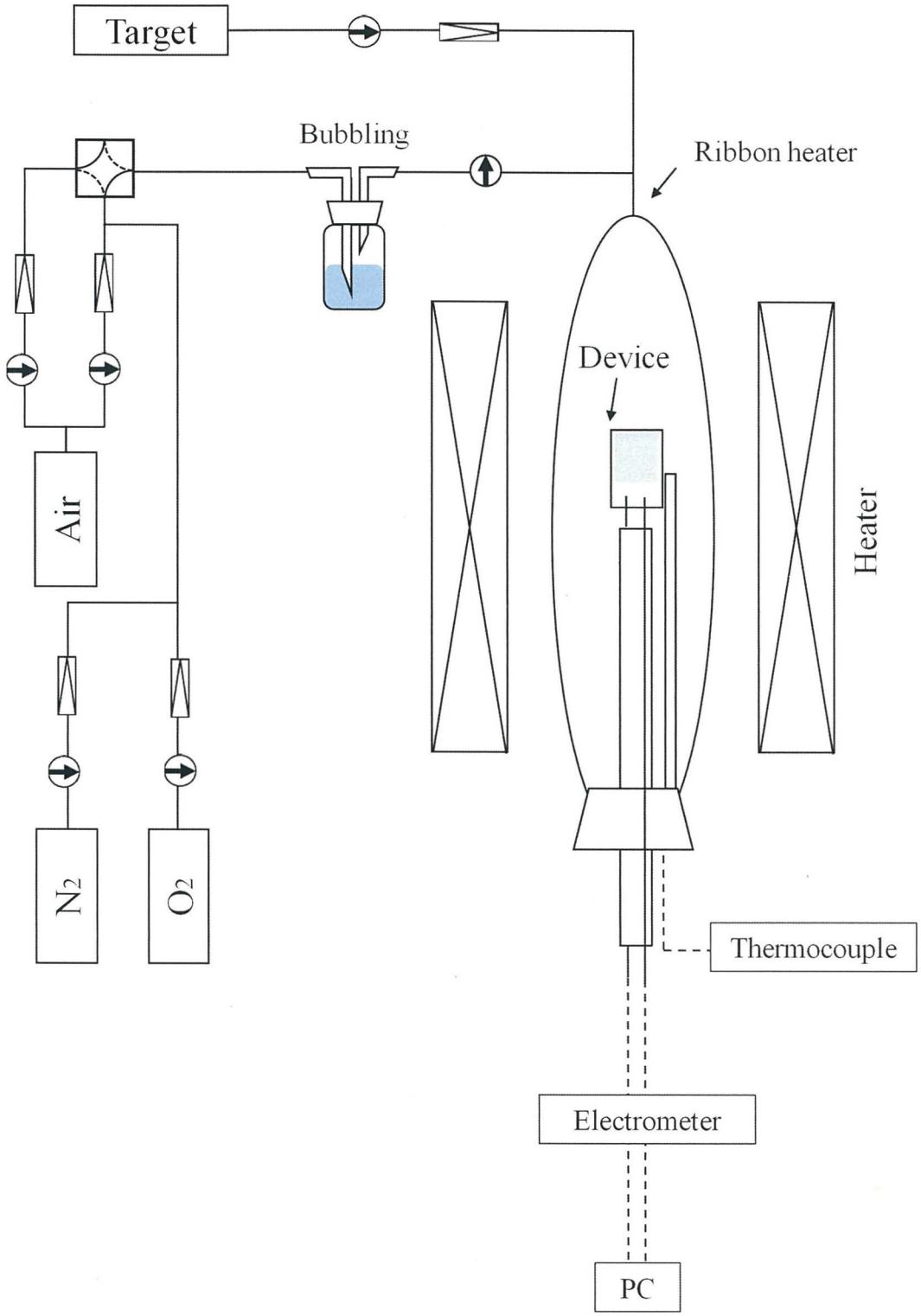

Figure 2.5 Schematic diagram of the electrical resistance value measuring device

2.4.3. Measuring method

First, pretreatment must be performed. It is known that the tin oxide gas sensor adsorbs a gas such as water vapor existing in the air and changes the resistance value. When gases such as water vapor, nitrogen oxides (NOx), and CO_2 remain on the surface of the device, the resistance value and sensor sensitivity of the device are the result of combining not only the measurement atmosphere but also the interfering gas in the atmosphere. Therefore, the adsorbent on the surface of the sensor element was removed by pretreating the sensor element before measuring the resistance value. At this time, the holding temperature must be at least the hydroxyl group desorption temperature of 400°C), Therefore, in this experiment, the holding temperature was set to 20 degrees lower than the calcination temperature and kept in dry air for 3 hours to ensure and immediately desorb the hydroxyl group. Figure 2.6 shows a schematic diagram of pretreatment at 500°C calcination.

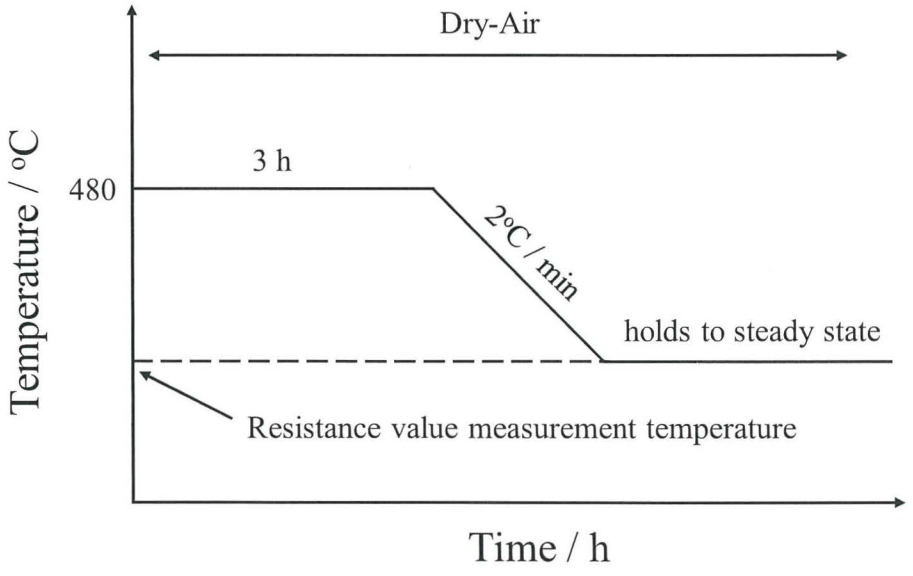

Fig 2.6 schematic diagram of pretreatment at 500°C calcination

2.4.4. Pore size distribution

SnO_2 paste was obtained by mixing the SnO_2 powder with an α-terpineol. This was thinly applied to aluminum foil and dried. The dried film was calcined and the pore distribution was evaluated by the nitrogen adsorption / desorption method.

2.5. Summary

In this chapter, tin oxide monodisperse sol was prepared using the preparation method used in our laboratory, and an attempt was made to prepare anisotropic tin oxide sol using additives. The method of physical property evaluation and the measurement method were also explained. Chapter 3 shows the evaluation of tin oxide, which is the prepared sensor material, and the effects of additives, and Chapter 4 shows the results of the sensor characteristics of the device prepared in this chapter.

Chapter 3.

Evaluation of anisotropic SnO_2 nanoparticles

3.1. Introduction

In Chapter 1, the necessity of the design factors in this study, such as transducer function and crystal plane control were shown, in particular, the study on the exposed crystal plane of SnO_2 was in an inadequate state. This chapter will describe the fabrication of anisotropic SnO_2 nanoparticles and their material evaluation. Specifically, based on the method for preparing the SnO_2 nanoparticle dispersion sol shown in Chapter 2, the effect on the anisotropy of SnO_2 nanoparticles was evaluated by evaluating the surface state and pore distribution of the obtained SnO_2 nanoparticles.

In this chapter, we first attempted to synthesize SnO_2 nanoparticles by subjecting a tin acid gel dispersion whose pH was adjusted using TMAH to hydrothermal treatment. Then, the effect of adding an amine-based additive to the tin acid gel dispersion whose pH was adjusted using TMAH on the growth of SnO_2 crystals was examined.

3.2. Characteristics of SnO_2 nanoparticles

3.2.1. X-ray diffraction patterns

In this study, we investigated whether additives and calcination temperature affect the particle size. The tin acid sol whose pH was adjusted using TMAH was ordered as AI-SnO_2, and the sol which added an amine-based additive to the tin acid gel dispersion whose pH was adjusted using TMAH was ordered as I-SnO_2. The calcination temperatures were set to 400°C, 500°C and 600°C

Figure3.1 shows the XRD pattern of the SnO_2 nanoparticles calcined powder obtained under each preparation condition. From this, it was found that SnO_2 was obtained by hydrothermal synthesis because the XRD peak coincided with rutile-type SnO_2 (JCPDS: 411445). The result of calculating the crystallite sizes of each particles is shown in Table 3.1. In the previous research, we applied Sherrer's formula to evaluate crystallite sizes, but when the crystallite diameter exceeds 50 nm, the value exceeds the applicable range of Sherrer's formula. Therefore, the particle size is evaluated using the FP method in this research. As described in Chapter 2, in the FP method, the X-ray intensity of each

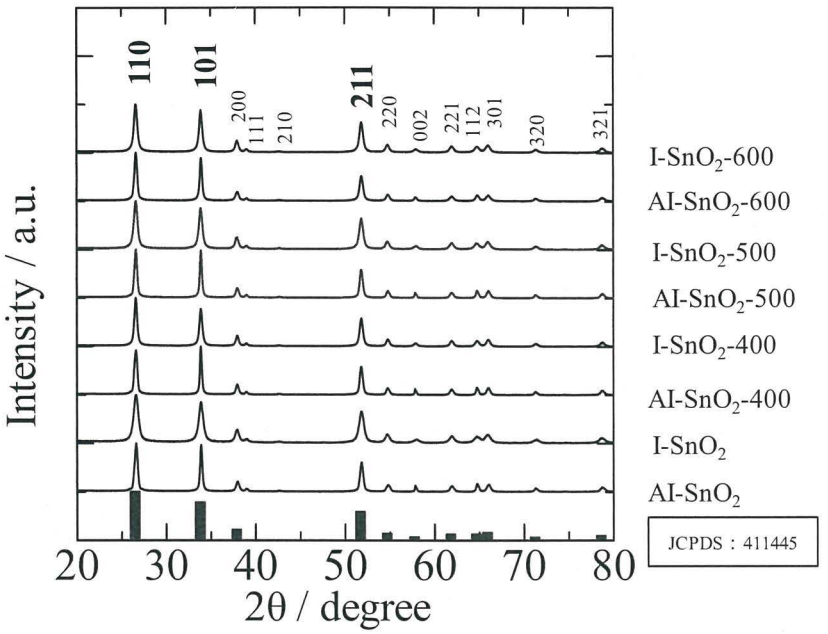

Figure 3.1 XRD pattern of each preparation condition of prepared SnO_2

Table 3.1 XRD pattern of each preparation condition of prepared SnO_2

sample	FP method / nm	
	ab	c
I-SnO_2	16.0	16.1
AI-SnO_2	24.1	57.1
I-SnO_2-400	26.1	26.8
AI-SnO_2-400	26.0	68.5
I-SnO_2-500	20.1	21.2
AI-SnO_2-500	27.5	50.0
I-SnO_2-600	22.3	24.8
AI-SnO_2-600	30.5	51.1

analytical element can be theoretically calculated from the physical constants such as the spectral distribution of the primary X-ray from the X-ray tube, the mass absorption coefficient, and the fluorescence yield. Therefore, the peak fitting and crystallite size distribution can be analyzed. Table 3.1 shows the results of the ab and c-axis lengths of the particles calculated by the FP method for comparison with the SEM results.

First, when we focus on the I-SnO_2 series in Table 3.1, it is inferred that the ab-axis and

c-axis lengths are approximately the same and were growing isotropically. On the other hand, since the length of the c-axis of AI-SnO_2 is significantly larger than that of the ab-axis, it is considered that AI-SnO_2 grows preferentially to [001] and has anisotropy. Next, the effect of the calcination temperature of AI-SnO_2 will be analyzed. As shown in Table 3.1, it was confirmed that after hydrothermal treatment AI-SnO_2 already has anisotropy. In addition, as the calcination temperature increases, the growth on the ab-axis increases, while the growth along the c-axis reaches its maximum at 400°C, and then tends to shrink. This suggests that SnO_2 gained sufficient energy up to 400°C and the crystals grew continuously. However, when the temperature exceeds 400°C, it is suggested that the SnO_2 atom recrystallizes at high temperature and changes its' position to reconstruct the surface, so the growth of the ab-axis increases while the growth of the c-axis shrinks. It is speculated that the same thing is happening with I-SnO_2 particles. From the above, it was found that the growth direction of the particles differs depending on the presence or absence of the additive. It is suggested that the introduction of the additive suppressed the anisotropic growth of the particles. It was also suggested that the sensitivity of the sensor may be improved by changing the size and crystal structure at different calcination temperatures.

3.2.2. Pore size and surface area of SnO_2 by BET method

Next, the specific surface area (BET method) and pore distribution (BJH method) were evaluated by using the nitrogen adsorption / desorption method for powders of AI-SnO_2, I-SnO_2 powders calcined at 400°C, 500°C and 600°C. Here, the pore distribution is shown in Figure 3.2, and the specific surface area, peak pore diameter and total pore volume are summarized in Table 3.2.

From the specific surface area results in Table 3.2, the specific surface area decreased as the calcination temperature of SnO_2 was increased. It was confirmed that it is consistent with the results of previous studies in our laboratory [56]. It is considered that this is because the specific surface area decreased due to slight crystal growth or particle agglutination caused by calcination. Further, it is considered that the pore diameter peak increased due to the same effect. Figure 3.2 Shows the pore distribution curves of AI-SnO_2, I-SnO_2 powders calcined at 400°C, 500°C and 600°C, respectively. The obtained sample has pores from 13.81 nm to 51.5 nm, and it is considered that the influence of the fine structure (gas diffusion pores) on the sensor sensitivity is small.

Table 3.2 specific surface area and pore radius peaks

sample	BET specific surface area [m^2/g]	Peak pore diameter [nm]	Total pore volume [cm^3/g]
I-SnO_2-400	34.1	24.4	0.2028
AI-SnO_2-400	24.6	13.81	0.1995
I-SnO_2-500	22.7	38	0.1754
AI-SnO_2-500	26.1	44.4	0.2140
I-SnO_2-600	22.7	51.5	0.2163
AI-SnO_2-600	13.3	32.6	0.0876

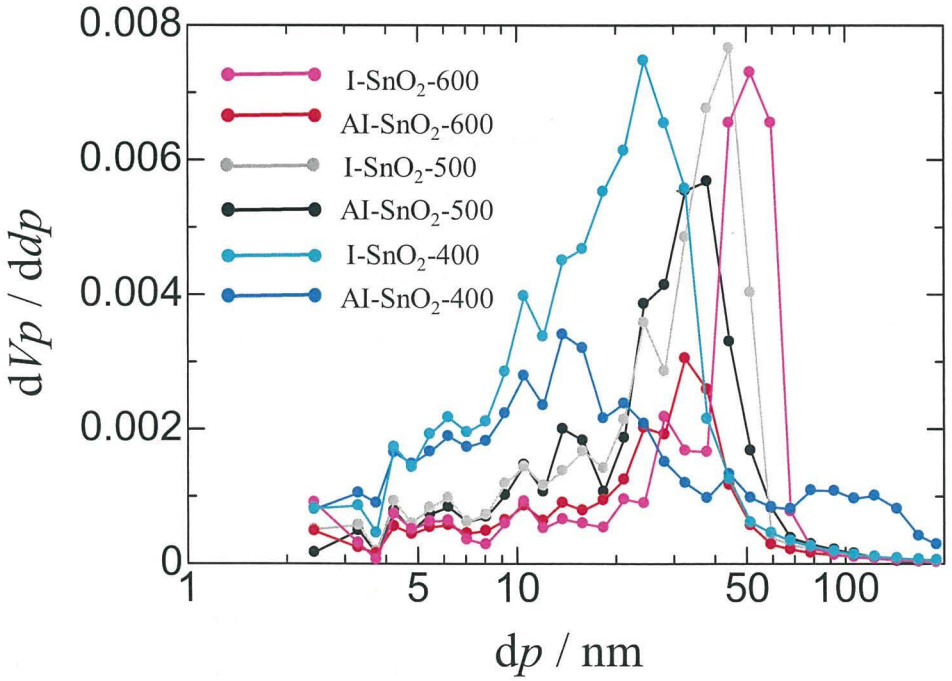

Figure 3.2 The pore distribution of each prepared SnO_2

3.2.3. Morphology evaluation by FE-SEM

FE-SEM observation was performed to verify the shape and diameter of the prepared SnO_2 nanoparticles. About 70 particles are randomly selected from each SEM image, and the results of the particle length and thickness distribution and the average value can be obtained. The SEM images and particle size distributions of AI-SnO_2, I-SnO_2 powders

calcined at 400°C, 500°C and 600°C prepared in this experiment are shown in Figures 3.3, 3.4 and 3.5, respectively. Table 3.3 summarizes the average particle length and width.

First, the changes in the average length, average width, average particle size with their calcination temperature of AI-SnO_2 and I-SnO_2 calculated from the SEM figure in Table 3.3, and it can be seen that the result roughly match the crystallite diameter estimated by the FP method. In addition, the average length and width of AI-SnO_2 did not change

Table 3.3 (a) Average particle length and width of AI-SnO_2

Sample	Average Length / nm	Average Width / nm
AI-SnO_2-400	67.3	17.5
AI-SnO_2-500	58.7	20.4
AI-SnO_2-600	54.4	21.1

Table 3.3 (b) Average size of I-SnO_2

Sample	Average size / nm
I-SnO_2-400	19.5
I-SnO_2-500	21.0
I-SnO_2-600	24.1

significantly as the calcination temperature increased, but it can be seen that the average size of I-SnO_2 increased. This is also consistent with the XRD results, suggesting that the introduction of additives suppressed the anisotropic growth of the particles.

According to Fig. 3.3, Fig. 3.4 and Fig. 3.5, the AI-SnO_2 series are rod-shaped anisotropic particles, and the I-SnO_2 series were observed that has become isotropically grown due to the addition of amine-based additives. It was found that the crystal growth direction could be controlled by additives. The control of the crystal growth direction by adding an additive during such hydrothermal synthesis is considered as follows. As for AI-SnO_2, when TMAH is adsorbed on (110), it inhibits the growth to [110] and crystal grows preferentially on [001]. On the other hand, in the case of I-SnO_2, when HDA coexists, it is considered that TMAH and HDA are adsorbed in all directions, the crystal growth rate in all directions decreases, and the crystal grows slowly isotropically.

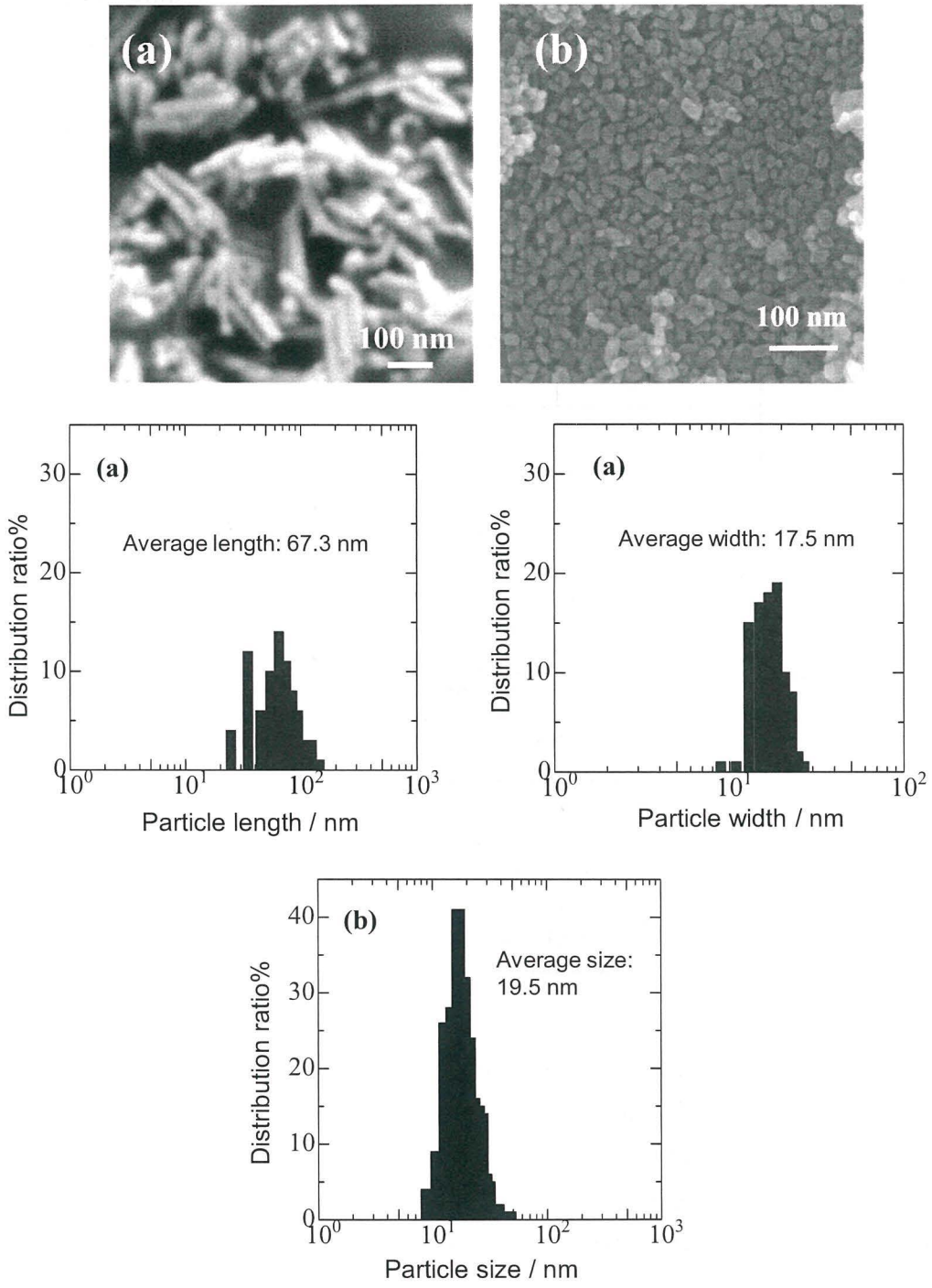

Fig 3.3 SEM image of SnO_2 and distribution of particle length, width and size (a)AI-SnO_2-400, (b) I-SnO_2-400

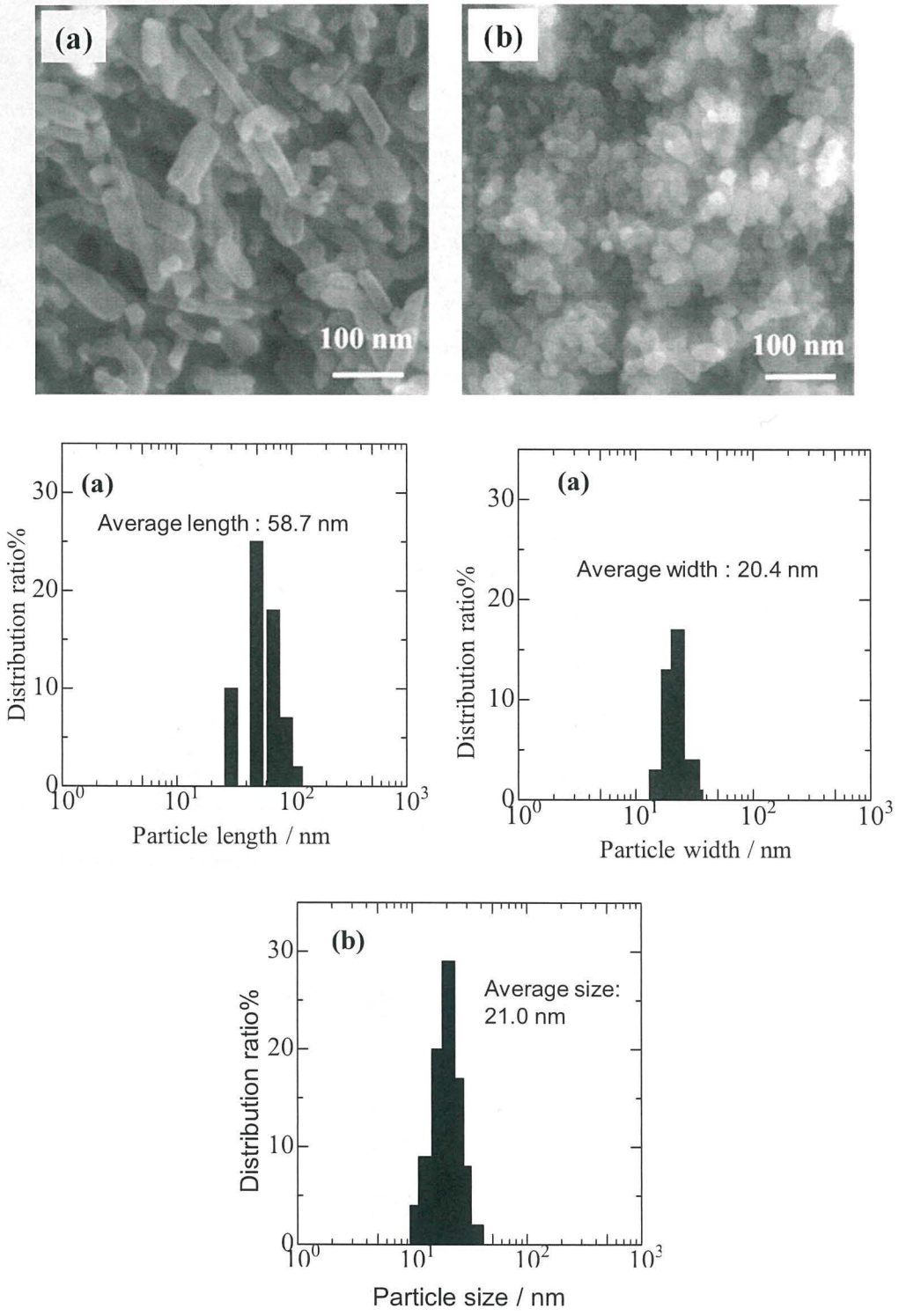

Fig 3.4 SEM image of SnO_2 and distribution of particle length, width and size (a)AI-SnO_2-500, (b) I-SnO_2-500

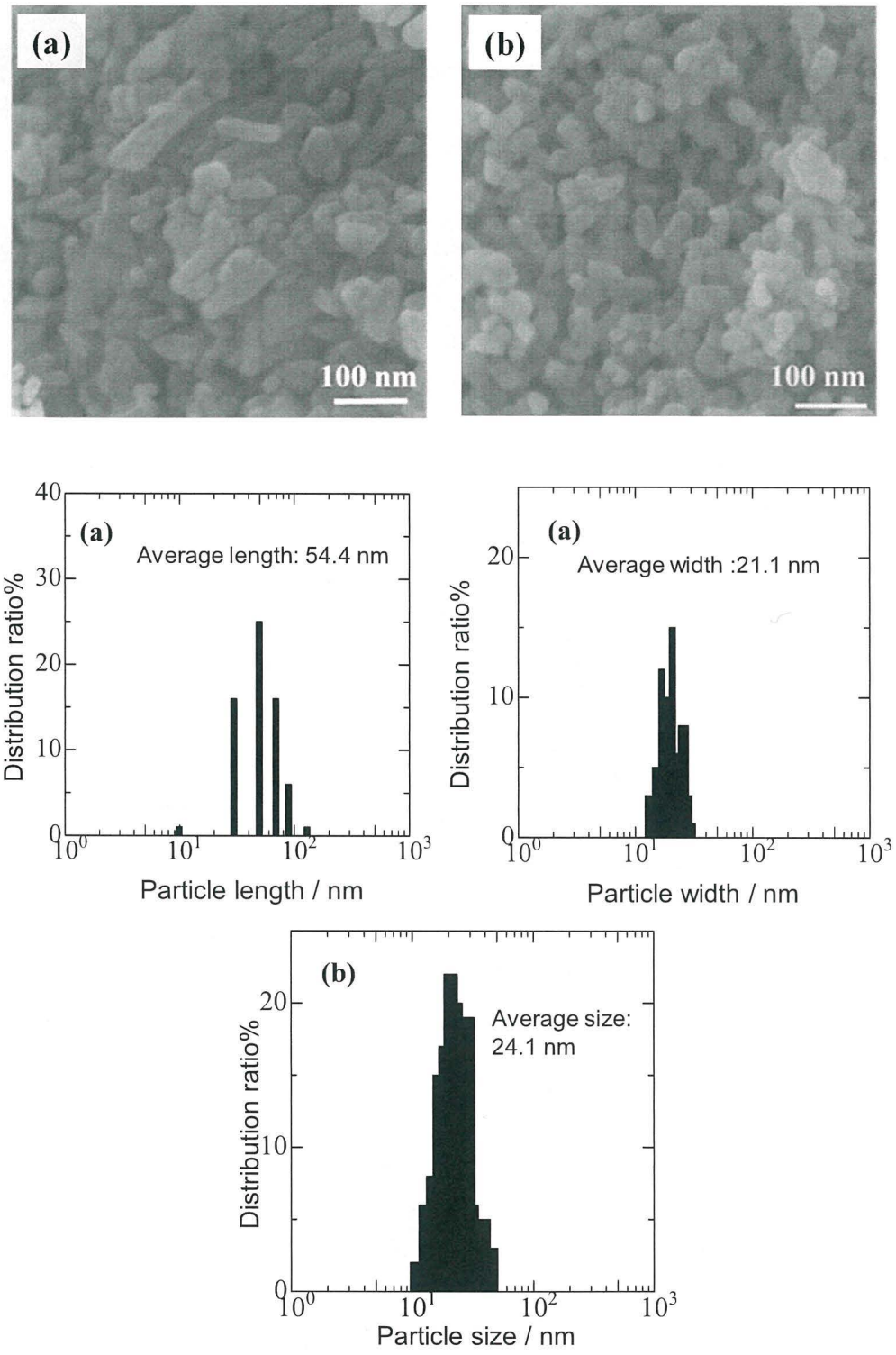

Fig 3.5 SEM image of SnO_2 and distribution of particle length, width and size (a)AI-SnO_2-600, (b) I-SnO_2-600

3.2.4. Morphology evaluation by TEM

So far, the surface condition and size of the particles have been evaluated, then a transmission electron microscope (TEM) was used to examine the size and shape of SnO_2 crystals and the proportion of exposed crystal planes and crystal planes. In this section, the plane spacing estimated from the TEM image and lattice fringes by observing AI-SnO_2-400 is shown in Fig. 3.6. A schematic diagram of the SnO_2 nanorod is shown in Figure 3.7. In Fig. 3.6 (a), the middle part of the tin oxide rod is taken, and almost even surface spacing is obtained in the middle part, and it can be estimated that the (110) surface is exposed. On the other hand, Fig. 3.6 (b) shows the end part of the rod, and it can be estimated that (101) and (200) are exposed. From this, it was clarified that AI-SnO_2 grew in the direction of [001], and SnO_2 nanoparticles with the (110) plane exposed on the side surface of the rod were obtained. Based on this result, AI-SnO_2-400 and I-SnO_2-400 were observed, and the ratio of the exposed rod surface evaluated by TEM image were shown in Fig. 3.8. From this, it can be seen that AI-SnO_2-400 was rod-shaped, and the proportion of rods was larger than that of I-SnO_2-400. It is considered that the exposure ratio of the (110) plane, the crystal plane which is constituting the rod portion is large. As described in Chapter 1, the effect of the crystal plane affects the sensor

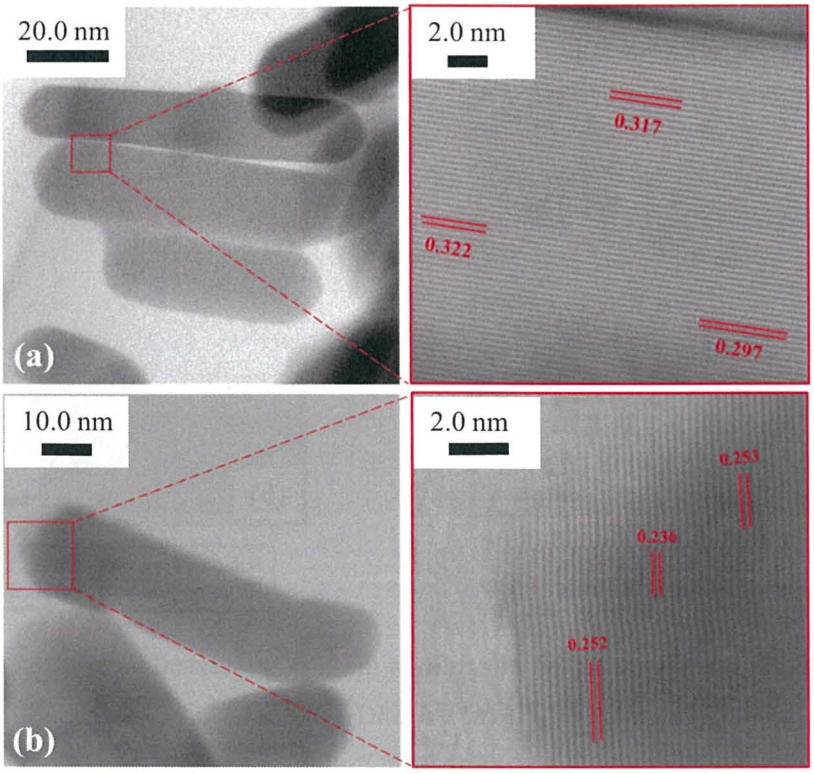

Figure 3.6 The TEM image of AI-SnO_2-400

sensitivity. From this, it can be expected that tin oxide having different anisotropy behaves differently in sensor sensitivity.

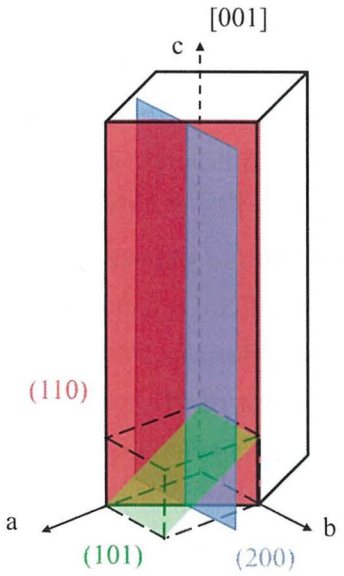

Figure 3.7 A schematic diagram of the SnO_2 nanorod

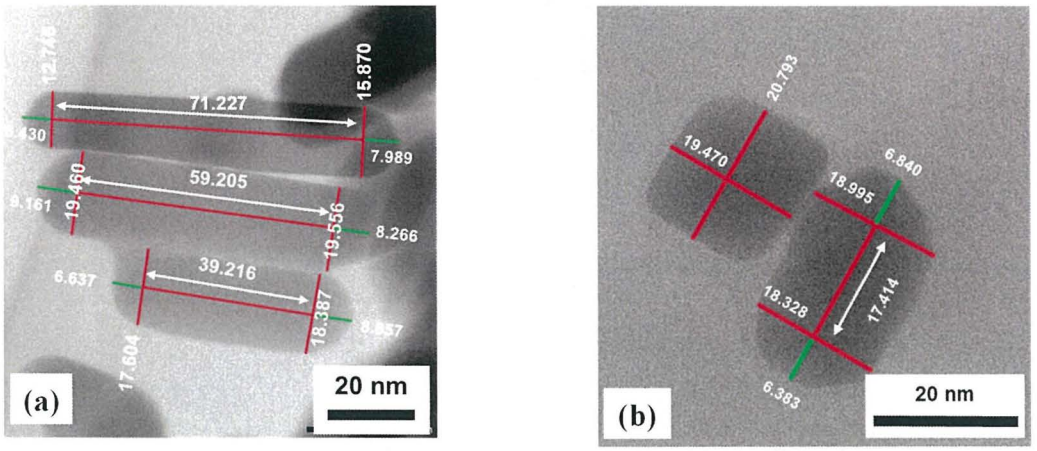

Ratio of Rod part: 57%
Ratio of End part : 43%

Ratio of Rod part: 46%
Ratio of End part : 54%

Figure 3.8 The ratio of the exposed crystal face

(a) AI-SnO_2-400

(b) I-SnO_2-400

3.2.5 Observation of sensor film thickness

The sample paste was applied to an alumina substrate with a comb-shaped metal electrode, and the thickness of the sensor element after calcination was evaluated. Table 3.4 summarizes the average film thickness of the sensor elements. From the measurement results, the film thickness of the sensor film was about 20 μm on average.

Table 3.4 Average film thickness of the sensor elements

Sample	Average film thickness / μm
I-SnO_2-400	18.0
AI-SnO_2-400	19.8
I-SnO_2-500	22.6
AI-SnO_2-500	25.2
I-SnO_2-600	23.0
AI-SnO_2-600	22.4

3.3. Summary

This chapter examined how additives and thermal treatment affect SnO_2 crystal growth. The results in this chapter investigated the effect of SnO_2 nanoparticles on anisotropic growth using amine-based additives. It is also suggested that the addition of the amine-based additive shortens the rod-shaped tin oxide and eliminates the anisotropy. This was confirmed by SEM and TEM observation. From the results of the specific surface area and pore distribution obtained by the BET method, it was found that the specific surface area decreased and the pore diameter increased as the calcination temperature increased. In the next chapter, the sensor response characteristics were evaluated using calcined AI-SnO_2 and I-SnO_2.

Chapter 4.

Effect of anisotropy of SnO_2 nanoparticles on sensor characteristics

4.1. Introduction

In order to investigate the effect of SnO_2 with amine-based additives on the electrical characteristics of the sensor and the effect of calcination temperature, the powders of AI-SnO_2 and I-SnO_2, which were evaluated in Chapter 3 were applied as materials. The sensor response characteristics to H_2, CO were evaluated to investigate the influence on gas response of different gas molecule sizes. Then the sensor response characteristics to ethanol were evaluated to investigate the influence on Gas response of gases with different reaction pathways. Based on the obtained results, the correlation between the sensor response characteristics and the anisotropy of SnO_2 was verified.

4.2. Sensor characterization of SnO_2

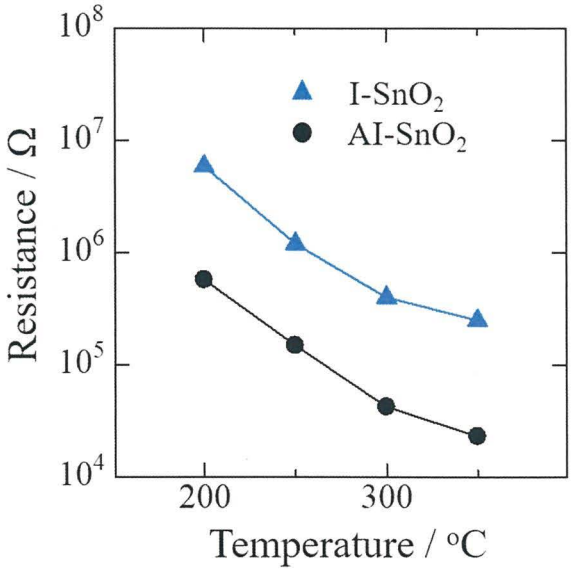

Figure 4.1 The operating temperature dependence of the electrical resistance value in air

In this section, the electrical resistance values in the air are shown using AI-SnO_2, I-SnO_2, which are SnO_2 nanoparticles with different anisotropies evaluated in Chapter 3. Figure 4.1 shows the operating temperature dependence of the electrical resistance value in air. From this, I-SnO_2 showed a higher electrical resistance value than AI-SnO_2. From the results of SEM, it is considered that AI-SnO_2 has a longer particle length than I-SnO_2, as shown in Fig 4.2, and therefore the number of interparticle interfaces between comb-shaped electrodes is small. In both the Schottky model and the tunnel conduction model shown in Chapter 1, the interparticle interface serves as an energy barrier to the movement of carrier electrons. Therefore, it is considered that I-SnO_2, which is considered to have many interparticle interfaces, will take more energy for electron mobility, showed a high electrical resistance value. However, since the rod lengths of the particles are different, it is possible that the volume resistance of the particles themselves is different.

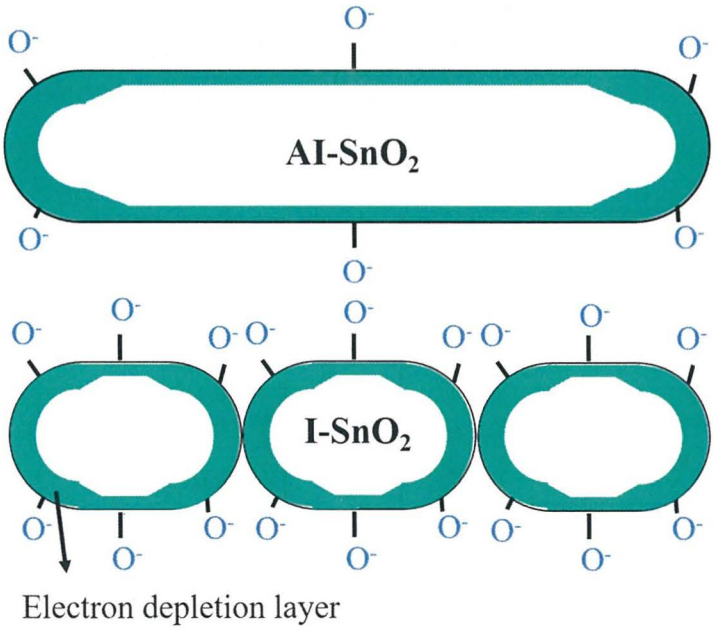

Figure 4.2 The model of oxygen adsorption on AI- SnO_2- 500 and I-SnO_2- 500

4.3. Gas response of different gas molecule sizes

Since tin oxide is an acidic oxide, it is thought that it easily reacts with gases such as H_2 and CO. In addition, H_2 and CO have different gas molecule sizes, but when they react with adsorbed oxygen on the tin oxide surface as shown in Equation 4.1 and 4.2, the number of oxygen consumed is the same, and It is thought that it might be a difference in sensor sensitivity due to differences in pore distribution and exposed crystal plane.

Therefore, in this section, AI-SnO_2-500 and I-SnO_2-500 nanoparticles, which have different anisotropy synthesized in Chapter 3, are used to detect the response to H_2 and CO, which consumed the same number of adsorbed oxygen for the surface reaction of the sensor.

Before evaluating the sensor response characteristics of each operating temperature, the sensor was refreshed for 3 h at 480°C under air circulation. After refreshing the sensor, the temperature was lowered to each operating temperature, and after sufficiently holding until the electric resistance value in the air became stable, H_2 having a predetermined concentration was introduced. The sensor operating temperature was evaluated at 200, 250, 300, and 350°C, and the sensor response characteristics for 200, 400, 600, 800, and 1000 ppm H_2 were evaluated. Figure 4.3 shows the response curve of the sensor to H_2. Figure 4.4 shows the operating temperature dependence of the sensor sensitivity of AI-SnO_2-500 and I-SnO_2-500 for 200 ppm H_2. Figure 4.5 shows the relationship between the sensor sensitivity to H_2 and the H_2 concentration.

$$H_2 + 1/2O_2 \rightarrow H_2O \qquad (4.1)$$

$$CO + 1/2O_2 \rightarrow CO_2 \qquad (4.2)$$

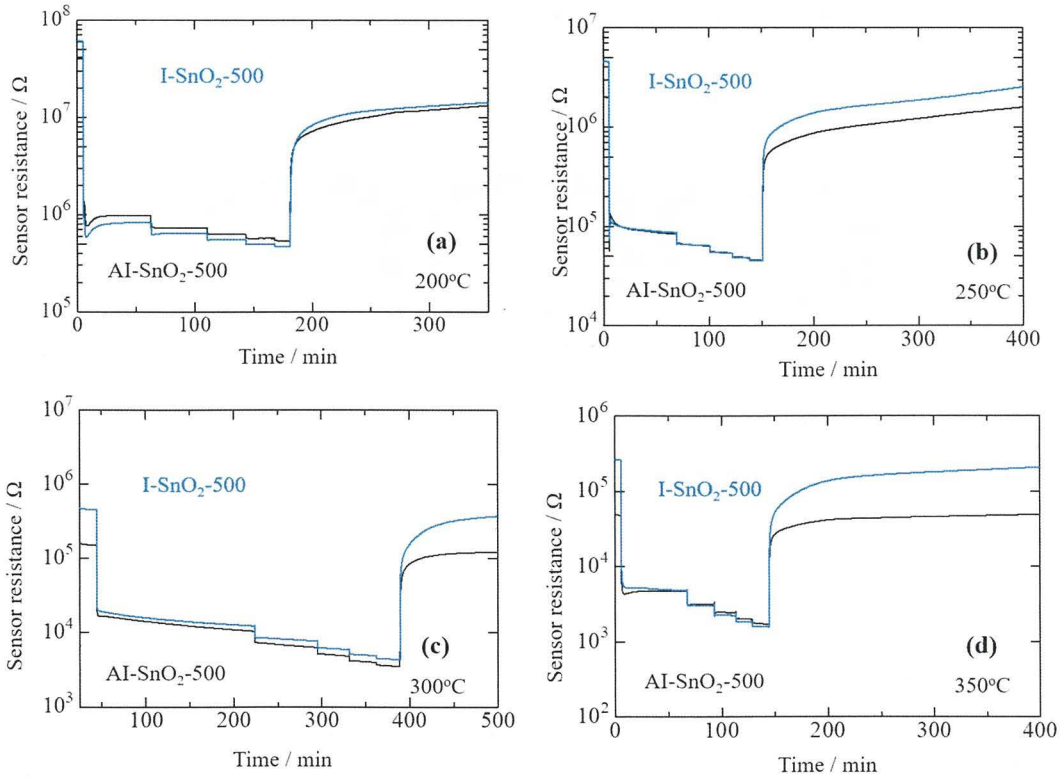

Figure 4.3 The response curve of the sensor to H_2

(a) 200°C、(b) 250°C、(c) 300°C、(d) 350°C

From Figure 4.3, we can know in the case of H_2 detection, I-SnO_2-500 took longer to stabilize the electric resistance value than AI-SnO_2-500. From the nitrogen adsorption / desorption measurement results, it is considered that the time required for the diffusion of H_2O produced by the reaction between H_2 and adsorbed oxygen is about the same because the pore diameters of these particles are both over 20 nm. From this, the difference of the time required for the electrical resistance value to stabilize differs between AI-SnO_2-500and I-SnO_2-500 is caused by the time required for H_2O to be adsorbed on the SnO_2 surface is different. It is also clear that as the operating temperature decreases, the time required to stabilize in H_2 / air increases. This suggests that H_2O is likely to be desorbed when measured at high temperatures, and that H_2O may be adsorbed and difficult to be desorbed at low temperatures.

From Figure 4.4, I-SnO_2-500 showed higher sensor sensitivity than AI-SnO_2-500 at any temperature. This is a result suggesting that AI-SnO_2 obtained in this study is considered to have a high exposure ratio of (110) due to its shape, and I-SnO_2 is expected to have a higher exposure ratio other than (110) than AI-SnO_2. As for SnO_2, the surface energy of (110) is the lowest and stable, so the other surface is considered to be the active surface showing the sensor response. Therefore, it is considered that I-SnO_2 exposes more crystal planes that are active sites of the sensor reaction than AI-SnO_2, and it is presumed that the sensor sensitivity to hydrogen has increased.

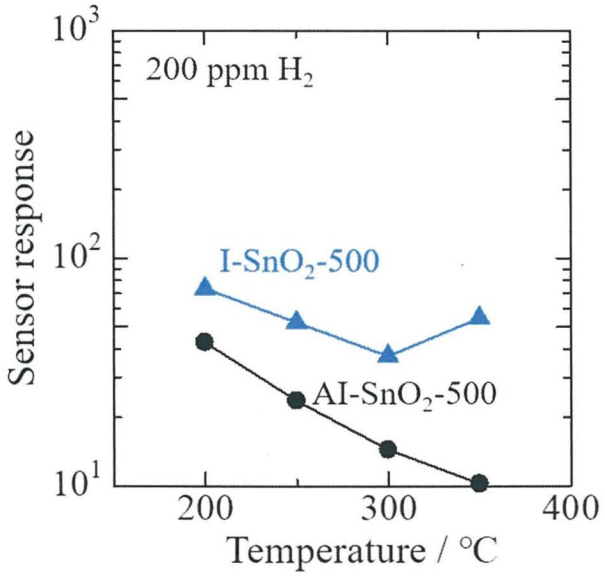

Figure 4.4 The operating temperature dependence of the sensor sensitivity of AI-SnO_2-500 and I-SnO_2-500 for 200 ppm H_2.

Next, From Fig. 4.5, it can be seen that the sensor sensitivity increases as the H_2 concentration increases, and that the H_2 concentration and the sensor sensitivity have a linear relationship.

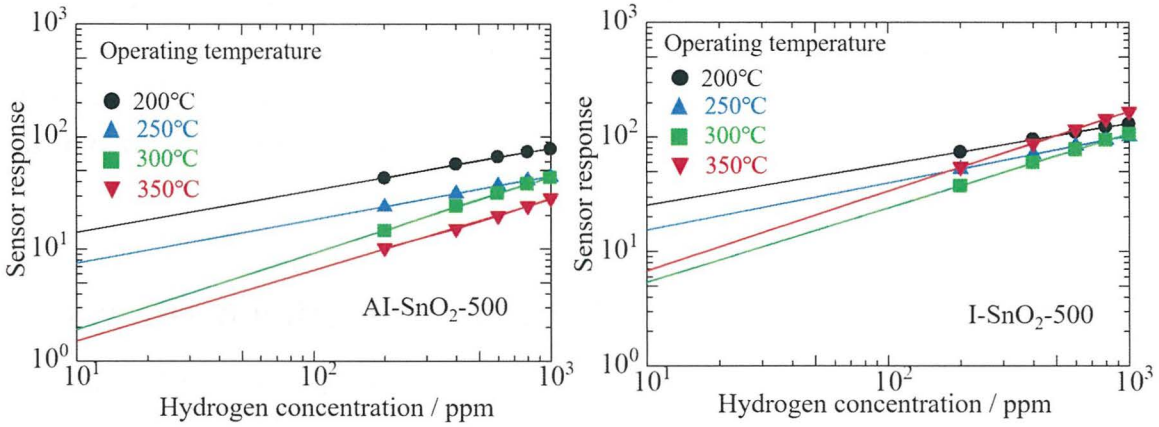

Figure 4.5 The operating temperature dependence of the sensor sensitivity of AI-SnO_2-500 and I-SnO_2-500 for 200 ppm H_2.

On the other hand, the sensor operating temperature of CO was evaluated at 150, 200, 250, 300, and 350°C, and the sensor response characteristics for 200, 400, 600, 800, and 1000 ppm CO were evaluated. Fig. 4.6 shows the operating temperature dependence of

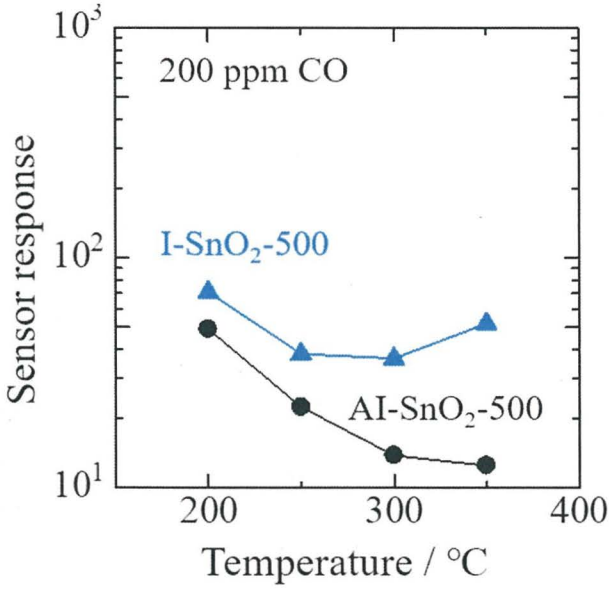

Figure 4.6 The operating temperature dependence of the sensor sensitivity of AI-SnO_2-500 and I-SnO_2-500 for 200 ppm CO.

the sensor sensitivity of AI-SnO_2-500 and I-SnO_2-500 on 200 ppm CO. From this, the operating temperature dependence of the sensor sensitivity with respect to the same concentration of H_2 and CO had similar sensing behavior. As with H_2, it is considered that SnO_2-HDA-500 showed high sensitivity because there are many reaction sites on the crystal plane corresponding to the rod end and the reaction activity between H_2 and adsorbed oxygen is high. The pore diameters of both AI-SnO_2-500 and I-SnO_2-500 are 20 nm or more, and it is considered that the diffusion of gas molecules of H_2 and CO is about the same. Therefore, the difference in sensitivity of the materials is considered to be the effect of the crystal plane.

4.4. Gas response of gases with different reaction pathways

In the previous section, we discussed the sensor sensitivity of gases with the same reaction pathway but different sizes used the devices of tin oxide with different anisotropies. In this section, the sensitivity to ethanol, which is a gas with a different reaction pathway, was measured. Ethanol (C_2H_5OH) is a larger molecule than H_2 and is thought to be easily adsorbed on the particle surface at low temperatures due to its high polarity. Therefore, it is considered that the sensor response characteristic strongly depends on the exposed crystal plane and its size. The sensor response characteristics to C_2H_5OH were evaluated using AI-SnO_2-500 and I-SnO_2-500. The sensor operating temperature was 150, 200, 250, 350°C, and the C_2H_5OH concentration was 20,40,60,80,100 ppm.

Figure 4.7 shows the operating temperature dependence of the sensor sensitivity on 20 ppm C_2H_5OH. As a result, AI-SnO_2-500 has a high sensor sensitivity at 200°C or less. Abokifa et al. calculated the binding energy with ethanol on the (110) and (101) planes, and reported that the (110) plane had a higher binding energy with ethanol [39]. This suggests that ethanol is easily adsorbed on the (110) plane. As shown in the Figure 4.8, at low operating temperatures, oxygen is adsorbed more on the edge surface of the cubic particle I-SnO_2, and an electron depletion layer is formed, and even if ethanol is adsorbed later, it is conceivable that the resistance does not decrease so much. On the other hand, AI-SnO_2, which is a rod-shaped particle, showed high sensitivity because the edge surface was less exposed. In addition, the sensitivities between AI-SnO_2-500 and I-SnO_2-500 were switched above 200°C, resulting in I-SnO_2-500 taking higher sensitivities. This is because the amount of adsorbed oxygen increases as the operating temperature increases and the reaction with ethanol proceeds, as shown in the Figure 4.9.

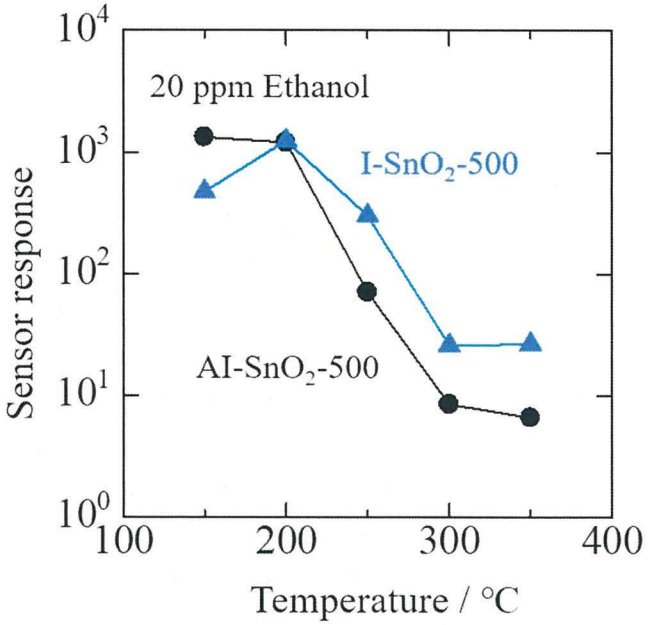

Figure 4.7 The operating temperature dependence of the sensor sensitivity of AI-SnO_2-500 and I-SnO_2-500 for 20 ppm Ethanol.

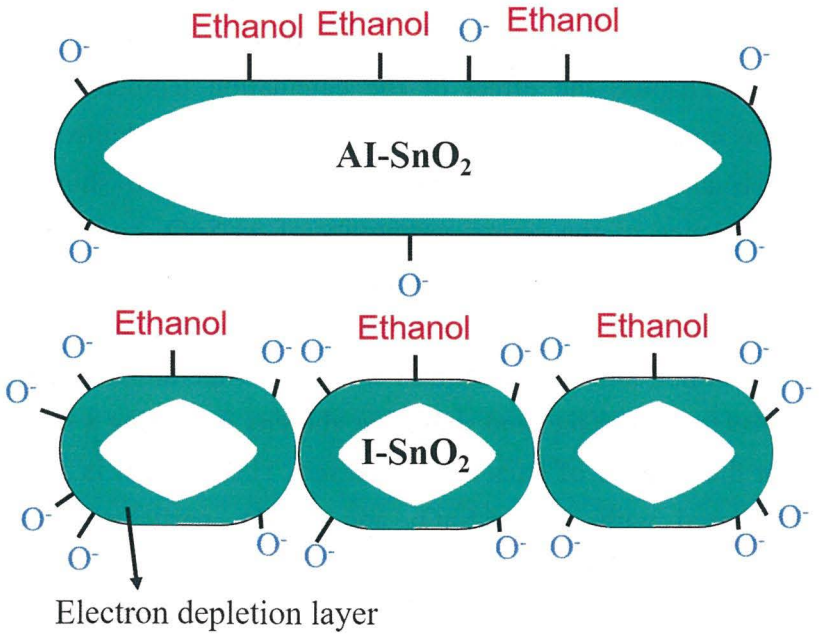

Figure 4.8 The model of adsorption state on AI- SnO_2 and I-SnO_2

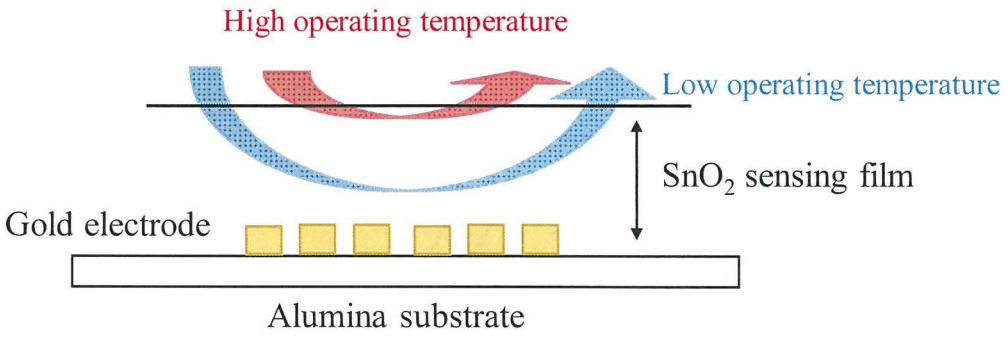

Figure 4.9 The model of reaction at different temperature on sensor surface

Therefore, it is considered that I-SnO_2-500, which exposes many edge surfaces that can adsorb oxygen, showed high sensor sensitivity. Since ethanol reacts on the surface, it does not reach the inside of the membrane, so it is probable that a significant decrease in sensor sensitivity was observed above 200°C.

4.5. The effect of calcination temperature on sensor characteristics

4.5.1. Gas response of SnO_2 calcined at different temperature on 200 ppm H_2

From Chapter 1, it was found that the surface condition of the material affects the sensor sensitivity. In this chapter, the effect of the calcination temperature on the sensor characteristics was investigated from the sensitivity of tin oxide calcined at 400°C, 500°C, and 600°C to H_2 and the sensor characteristics. Figure 4.10 shows the operating temperature dependence of the sensor sensitivity of AI-SnO_2 and I-SnO_2 calcined at different temperature on 200 ppm H_2. From this, the higher the calcination temperature, the lower the sensitivity. As discussed in Chapter 3, when the calcination temperature exceeds 400°C, the SnO_2 atom recrystallizes at a high temperature, and then changes its position, reconstructs the surface, and stabilizes, thereby indicating a sensor response. It is presumed that the number of sites has decreased. Therefore, it is suggested that the same thing happened with the AI-SnO_2 and I-SnO_2 particles as the calcination temperature increased, and the sensitivity decreased.

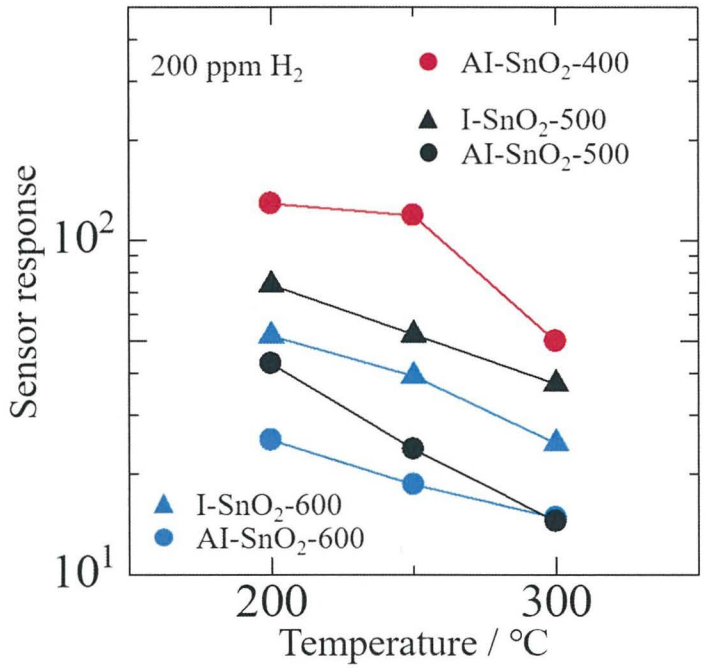

Figure 4.10 The operating temperature dependence of the sensor sensitivity of SnO_2 calcined at different temperature on 200 ppm H_2.

4.5.2. Gas response of SnO_2 calcined at different temperature on 20 ppm Ethanol

Figure 4.11 shows the operating temperature dependence of the sensor sensitivity on 20 ppm C_2H_5OH of a SnO_2 calcined at 400°C, 500°C and 600°C. Here, the sensor measurement temperature for 20 ppm C_2H_5OH of the sample calcined at 400°C was set to in the low temperature region of 150,200,250°C. As a result, AI-SnO_2-400 maintained high sensor sensitivity at 200°C or less. On the other hand, All sensitivities showed a significant decrease in sensor sensitivity below 200°C. This has the same tendency as the sensor sensitivity of the sample calcined at 500°C.

Compared with the results of SnO_2 which calcined at high temperature, it was found that the sensitivity of the sample calcined at 400°C was higher. It is considered that SnO_2-400°C, which has a lower calcination temperature, has an incomplete tin oxide surface composition and has more reaction sites. In addition, It is considered that absorbed oxygen decreased when calcination temperature increased. Therefore, it is considered that more ethanol was adsorbed on the surface of SnO_2-400°C and the sensor sensitivity was

high.

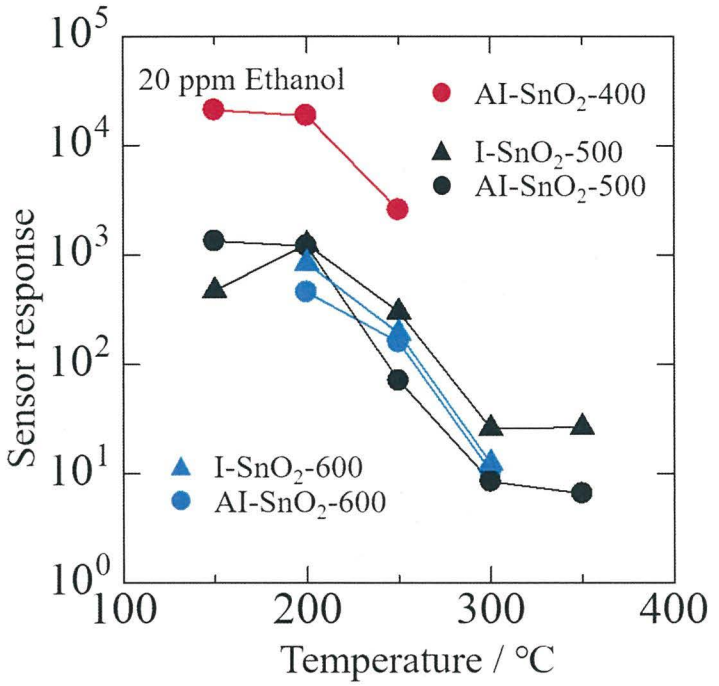

Figure 4.11 The operating temperature dependence of the sensor sensitivity of SnO_2 calcined at different temperature on 20 ppm Ethanol.

4.6. Summary

In this chapter, the electrical characteristics and sensor response characteristics of the sensor were evaluated using AI-SnO_2 and I-SnO_2 calcined at 500°C. AI-SnO_2-500 shows lower electrical resistance value in the air. In addition, the sensor sensitivity for H_2 and CO was higher in I-SnO_2-500 than in AI-SnO_2-500. This suggests that the surface reaction active site is at the rod end part. On the other hand, with respect to ethanol, AI-SnO_2-500 showed high sensitivity at a low operating temperature of 200°C or less, and a significant decrease in sensor sensitivity was observed above 200°C. From this result, it is considered that the surface combustion reaction occurs in the high temperature region and the sensitivity is lowered. AI-SnO_2-500 has a high sensor sensitivity at 200°C or less. It is considered that the surface adsorption of C_2H_5OH strongly contributes to the sensor sensitivity at low operating temperature. Therefore, it is considered that AI-SnO_2, which

exposes a large amount of the (110) plane, adsorbed more ethanol and showed high sensor sensitivity. Finally, by comparing the sensor characteristics of materials with different calcination temperatures, it was found that the calcination temperature affects the crystal plane of the material and the sensor sensitivity. From the above results, it was suggested that the exposed crystal plane of SnO_2 nanoparticles strongly influences the sensor response characteristics and is an effective factor in material design.

Chapter 5

Conclusions

So far, our laboratory has examined the receptor function, transducer function, and utilization efficiency of the sensor membrane as material design factors for increasing the sensitivity of semiconductor gas sensors, and has proposed material design guidelines that combine these factors. In this paper, in order to verify the specificity of the crystal plane, which is a candidate for a new material design factor, we synthesized anisotropic SnO_2 nanoparticles and attempted to elucidate the relationship between the sensor response characteristics and the crystal plane.

In Chapter 1, we explained the gas detection mechanism of SnO_2 semiconductor gas sensors and the material design factors of gas sensors that our laboratory has proposed so far. We also explained the crystal plane control method of oxide nanoparticles and the influence of the crystal plane on the sensor response characteristics, which have been reported in recent years.

In Chapter 2, we explained the method for synthesizing SnO_2 and the method for evaluating the obtained materials in this study. In addition, the fabrication of the sensor element and the method of measuring the electrical resistance value were explained.

In Chapter 3, the physical properties of the prepared SnO_2 nanoparticles and the anisotropy control guideline were evaluated and verified. By the method proposed in this paper, we succeeded in synthesizing highly anisotropic rod-shaped SnO_2 nanoparticles. In other words, it was confirmed that it is an effective method for controlling the size of nanoparticles and the anisotropy of particles by adjusting the additives and the calcination temperature. In addition, the exposed crystal plane of the obtained anisotropic SnO_2 nanoparticles was the (110) plane, and it was confirmed that the exposure ratio was large.

In Chapter 4, the sensor response characteristics of the prepared sample were evaluated. Sensor response characteristics to H_2, CO and C_2H_5OH were evaluated using two types of SnO_2 nanoparticles with different anisotropy.

・For H_2 and CO detection, I-SnO_2-500 with a short rod length showed high sensor sensitivity. It was considered that the crystal planes constituting the rod ends are involved in the sensor response that governs oxygen adsorption and gas reaction.

・For C_2H_5OH detection, AI-SnO_2-500 with a long rod length showed high sensor sensitivity in the low operating temperature range of 200°C or less. It was clarified that C_2H_5OH, which is a polar molecule, adsorbs on the surface of SnO_2 particles and expresses a sensor response. On the other hands, there is a significant decrease in sensor

sensitivity was observed above 200°C. This is because the amount of adsorbed oxygen increases as the operating temperature increases and the reaction with ethanol proceeds, and ethanol does not reach the inside of the membrane.

As described above, by evaluating the sensor response characteristics using SnO_2 nanoparticles with different anisotropy, the crystal plane control of SnO_2 is one of the important material design guidelines for improving the sensor response characteristics. Became clear.

Acknowledgements

I would like to extend my deep gratitude to all those who have offered cordial and selfless support in writing this thesis.

My deepest gratitude goes first and foremost to Prof. Kengo Shimanoe, my supervisor, for his constant encouragement and guidance. He has walked me through all the stages of the writing of this thesis. Without his consistent and illuminating instruction, this thesis could not have reached its present form.

Second, I would like to express my heartfelt gratitude to all of my teachers who gave me a lot of academic and life guidance. Especially Prof. Ken Watanabe, Dr. Suematsu and Mrs. Hisadomi.

My sincere thanks also go to all the former and present members in laboratory: Mrs. Hoshino, Mrs. Shinagawa, Dr. Okuda, Mrs. Hiroyama, Mr. Uchiyama, Mr. Masumoto, Mr. Ichinose, for the encouraging words and time in listening to me and helping me work out my problems during the difficult course of the thesis. I also feel grateful to all other fellows: Mr. Ueda, Mr. Takeno, Mr. Mitamura, Mr. Matsumoto, Mr. Tashiro, Mr. Mikata, from whose help I benefited greatly.

Last my thanks would go to my beloved family for their loving considerations and great confidence in me all through these years in Japan. I am also grateful to my friends Ms. Fu, Ms. Xu, Mr. Wen, Mrs. Mori and Ms. Liu, for giving valuable suggestions and supporting me spiritually through my life.

Referance

(1) 株式会社石油産業新聞社「歴史を綴ったエピソード」
http://www.sekiyusangyo.co.jp/news/rekishi/rekisshi01.html

(2) T. Seiyama, A. Kato, K. Fujiishi, M. Nagatani, *Anal. Chem.*, **34**, 1502 (1962).

(3)田口尚義、特公昭 45-38200(出願昭 37).

(4) フィガロ技研株式会社，フィガロの歩み，https://www.figaro.co.jp/company/history.html

(5)ガスセンサの進歩と新たな応用
http://www.scej.org/docs/publication/journal/backnumber/8108-open-article.pdf

(6)株式会社メムス･コアホームページ
(http://www.mems-core.com/service/mems.html)

(7)平成２５年度 産業動向調査報告書 環境センサネットワークの産業動向と今後 の展望、一般財団法人マイクロマシンセンター産業動向委員会
(http://mmc.la.coocan.jp/research/report/report-list/PDFreportMokuji/2013_02.pdf)

(8) Gas Sensor
(https://baike.baidu.com/item/%E6%B0%94%E4%BD%93%E4%BC%A0%E6%84%9F%E5%99%A8/5691956?fr=aladdin)

(9) 厚生省 快適で健康的な住宅に関する検討会議(1997)

(10)清山哲郎、化学センサ実用便覧、フジ・テクノシステム (1986)

(11) エフアイエス株式会社 2011 年 (http://www.ikegin-c.jp/pdf/frm1111292.pdf)

(12) NISSHA 株式会社(https://www.nissha.com/products/allproducts/gas.html)

(13) 清山哲郎ほか編、化学センサー、講談社 (1982 年 3 月).

(14) Y. J. Chen, L. Nie, X.Y. Xue, Y.G. Wang, T.H. Wang, *Appl. Phys. Lett.*, **88**, 083105 (2006).

(15) Semiconductor gas sensor, ceramics **43**, No.5 (2008).
(http://www.ceramic.or.jp/museum/contents/pdf/2008_05_05.pdf)

(16) 末松昂一, 博士論文, SnO_2 ナノ粒子を用いた半導体ガスセンサの応答メカニズムに関する研究, (2012)

(17) N. Yamazoe, J. Fuchigami, M. Kishikawa, T. Seiyama, *Surf. Sci.*, **86**, 335-344 (1979).

(18) P. K. Clifford, D.T. Tuma, *Sens. Actuator.*, **3**, 233-254 (1982).

(19) Y. Mizokawa, S. Nakamura, *Jpn. J. Appl. Phys.*, **14**, 779-788 (1975).

(20) K. Suematsu, M. Yuasa, T. Kida, N. Yamazoe, K. Shimanoe, *J. Electrochem. Soc.*, **161**, B123-B128 (2014).

(21) K. Suemtasu, N. Ma, K. Watanabe, M. Yuasa, T. Kida, K. Shimanoe, *Sensors.*, **18**, 254 (2018).

(22) Noboru Ichinose, Yuji Yokomizo, Masaki Katsura, Institute of Electrical Engineers of Japan, Electronic Equipment Study Group Materials EDD-75-53 (1975).

(23) C. Xu, J. Tamaki, N. Miura, N. Yamazoe. *Sens. Actuator B.*, **3**, 147-155 (1991).

(24) Shoichi Tanaka, catalyst, **17**, 5, 141-148 (1975).

(25) H. Ogawa, M. Nishikawa, A. Abe, *J. Appl. Phys.*, **53**, 4448-4455 (1982).

(26) A. Rothschild, Y. Komen, *J. Appl. Phys.*, **95**, 6374-6380 (2004).

(27) N.Yamazoe, K. Shimanoe, *J. sensors.*, **2009**, 1-21 (2009).

(28) N. Yamazoe, K. Shimanoe, *Sens. Actuator B.*, **128**, 566-573 (2008).

(29) N. Yamazoe, K. Shimanoe, *J. Electrochem. Soc.*, **155**, J93 (2008).

(30) K. Suematsu, Y. Shin, Z. Hua, K. Yoshida, M. Yuasa, T. Kida, K. Shimanoe, *ACS Appl. Mater. Interfaces.*, **6**, 5319-5326 (2014).

(31) 山添昇, 電子技術, 25, 44(1983).

(32) N. Yamazoe, Y. Kurokawa, T. Seiyama, Sensors and Actuators, 4, 283-289(1983).

(33) L. Ma, W. Hu, Q. Pan, L. Zou, Z. Zou, K. Wen, H. Yang, Journal of CO2 Utilization, 34, 108-114(2019).

(34) L. Yao, Y. Li, Y. Ran, Y. Yang, R. Zhao, L. Su, Y. Kong, D. Ma, Y. Chen, Y. Wang, Journal of Alloys and Compounds 826, 154063(2020)

(35) L. Zhang, J. Shi, Y. Huang, H. Xu, K. Xu, Paul K. Chu, F. Ma., *ACS Appl. Mater. Interfaces.*, **11**, 12958 (2019).

(36) H. Yu, Y. Zhang, L. Dong, J. Wang., *Materials Science in Semiconductor Processing* 121, 105451(2021)

(37) N. Yamazoe, G. Sakai, K. Shimanoe, Catal. Surv. Asia., 7, 63-75, (2003).

(38) D. D. Vuong, G. Sakai, K. Shimanoe, N. Yamazoe, Sens. Actuators B, 105, 437-442(2005).

(39) Ahmed A. Abokifa, K. Haddad, J, Fortner, C S. Lo, P. Biswas., *J. Mater. Chem. A*, **6**, 2053 (2018).

(40) P. G. Choi, N. Izu, N. Shirahata, Y. Masuda., *Sensors & Actuators: B. Chemical 296, 126655 (2019)*

(41) D. H. Kim, W. -S. Kim, S. B. Lee, S. -H. Hong, *Sens. Actuators B.*, **147**, 653-659 (2010).

(42) Y. V. Kaneti, Z. J. Zhang, J. Yue, Q. M. D. Zakaria, C. Y. Chen, X. C. Jiang, A. B. Yu, *Phys. Chem. Chen. Phys.*, **16**, 11471-11480 (2014).

(43) J. Q. Xu, Z. G. Xue, N. Qin, Z. X. Cheng, Q. Xiang, *Sens. Actuators B.*, **242**, 148-157 (2017).

(44) N. Saito, K. Watanabe, H. Haneda, I. Sakaguchi, K. Shimanoe. *The Journal of Physical Chemistry C.* **122** (2018) 7353-7360

(45) R. Xu, L.X. zhang, M.W. L. *Sens. Actuators B.,* **289**,186-194 (2019).

(46) J. Zhang, S. Ohara, M. Umetsu, T. Naka, Y. Hatakeyama, T. Adschiri, *Adv. Mater.*, **19**, 203-206 (2007).

(47) J. Oviedo, M. J. Gillan., *Surf. Sci*, **463**, 93 (2000).

(48) D. H. Kim, W. -S. Kim, S. B. Lee, S. -H. Hong, *Sens. Actuators B.*, **147**, 653-659

(2010).
(49) J. Zhang, S. Ohara, M. Umetsu, T. Naka, Y. Hatakeyama, T. Adschiri, *Adv. Mater.*, **19**, 203-206 (2007).
(50) T. Adschiri, *The Micromeritics*., **60**, 24-32 (2017).
(51) Kida, K. Suematsu, K. Hara, K. Kanie, A. Muramatsu., *ACS Appl. Mater. Interfaces*., **8**, 35485 (2016).
(52) T. Kida, S. Fujiyama, K. Suematsu, M. Yuasa, K. Shimanoe, *J. Phys. Chem. C*., **117**, 17574 (2013).
(53) P. G. Choi, N. Izu, N. Shirahata, Y. Masuda., *ACS Appl. Nano Mater. 2, 1820−1827(2019)*
(54) P. Khaenamkaew, D. Manop, C. Tanghengjaroen, W. P. N. Ayuthaya, *Advances in Materials Science and Engineering,* (2020)
(55) Adsorption Seminar, Microtrac Bell Co., Ltd.
(https://www.microtrac-bel.com/tech/bel/entry6.html)
(56) 末松昂一, 修士論文, 結晶子径及びドナー密度を制御した SnO_2 ナノ粒子のセンサ特性, (2009)
(57) N. Yamazoe, G. Sakai, K. Shimanoe, *Cat. Surv. Asia*, **7**, 63-75(2003).

検討会資料 No. 14(最終検討会)　　2021.3.8　M2　梅　ウンテイ

異方性 SnO_2 のガス応答に対する焼成温度の効果

1. 実験目的

・焼成温度が SnO_2 の結晶化への影響調査。

2. 実験方法

乾燥、400℃焼成と600℃焼成したロッド状 SnO_2 粉末と850℃で焼成された試薬の SnO_2 粉末を用い、図1のような比率と手順でSiとメノウ乳鉢で 15 min ずつ混合、研磨することで、10 wt% Si を含有するSnO_2粉末を作った。得られた粉末を三つずつホルダーに圧着させてX線回折装置で測定し、得られたデータを定量分析した。また、得られた粉末をディスクにしてSEM-EDSによって定量分析を行った。

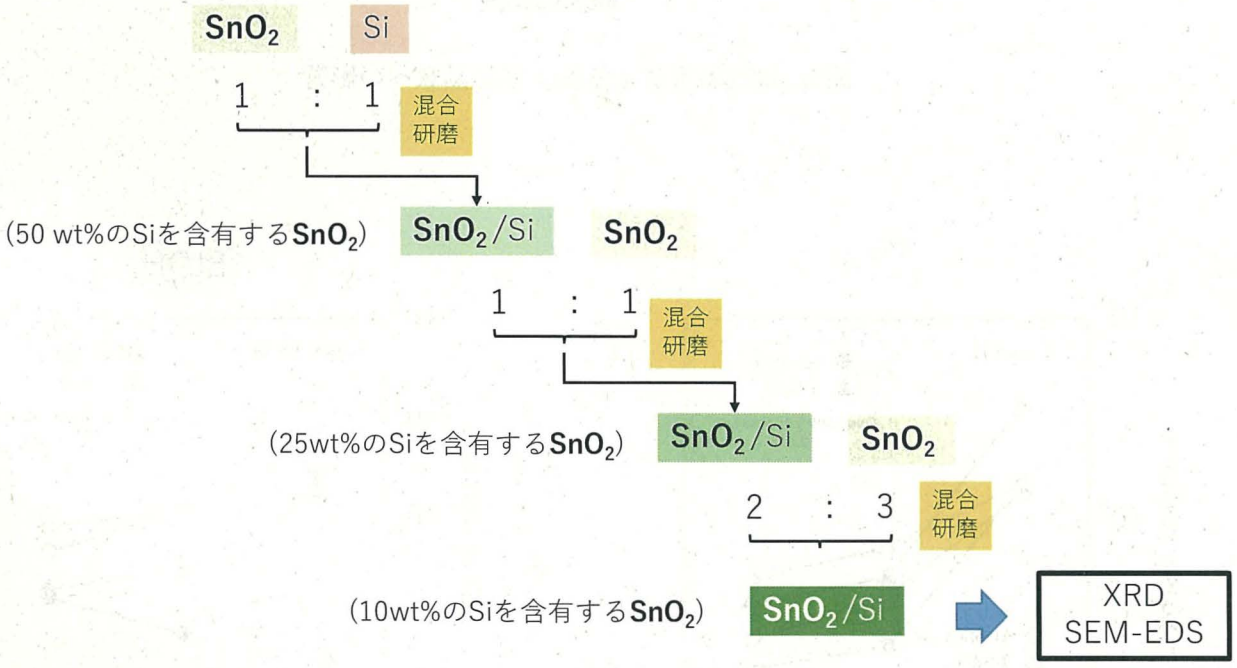

図 1. 実験の流れ

3. 結果と考察

XRD とSEM－EDSにより、測定された各サンプルの重量比と原子比はほぼ同じ程度の値を得られ、研磨により粉末が均一に混合できていると考えられる。図2に焼成温度による SnO_2 結晶数への影響を示す。これより、焼成温度の増加に伴い、SnO_2 の結晶数の割合が少なくなっていく傾向が現れる。また、図3のように焼成温度を増加させることで、H_2 とエタノールに対する感度が小さくなるという結果から、焼成温度の粒子成長に影響をあたえ、SnO_2の結晶数が少なくなり、表面構造が高温熱処理により再構成され、安定化され、表面におけるガス吸着特

性と反応活性が変化することで感度が低下したと示唆される。

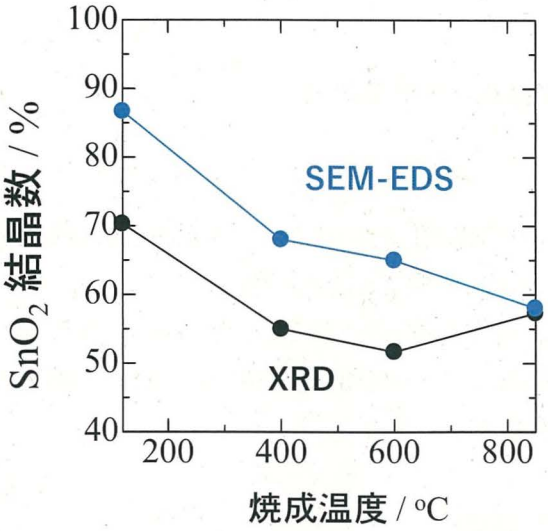

図 2. 焼成温度による SnO2 結晶数への影響

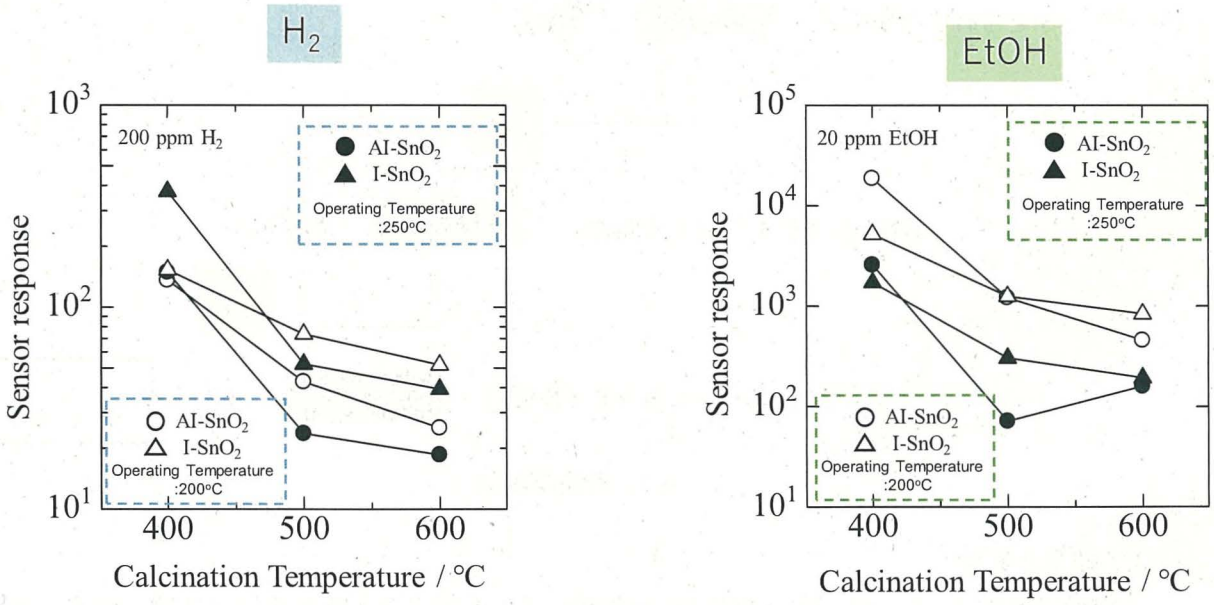

図 3. 焼成温度によるセンサ感度への影響

4. 今後の方針

・結晶面の制御によるガスセンサ感度の向上

・結晶の表面状態がガスセンサ感度への影響調査

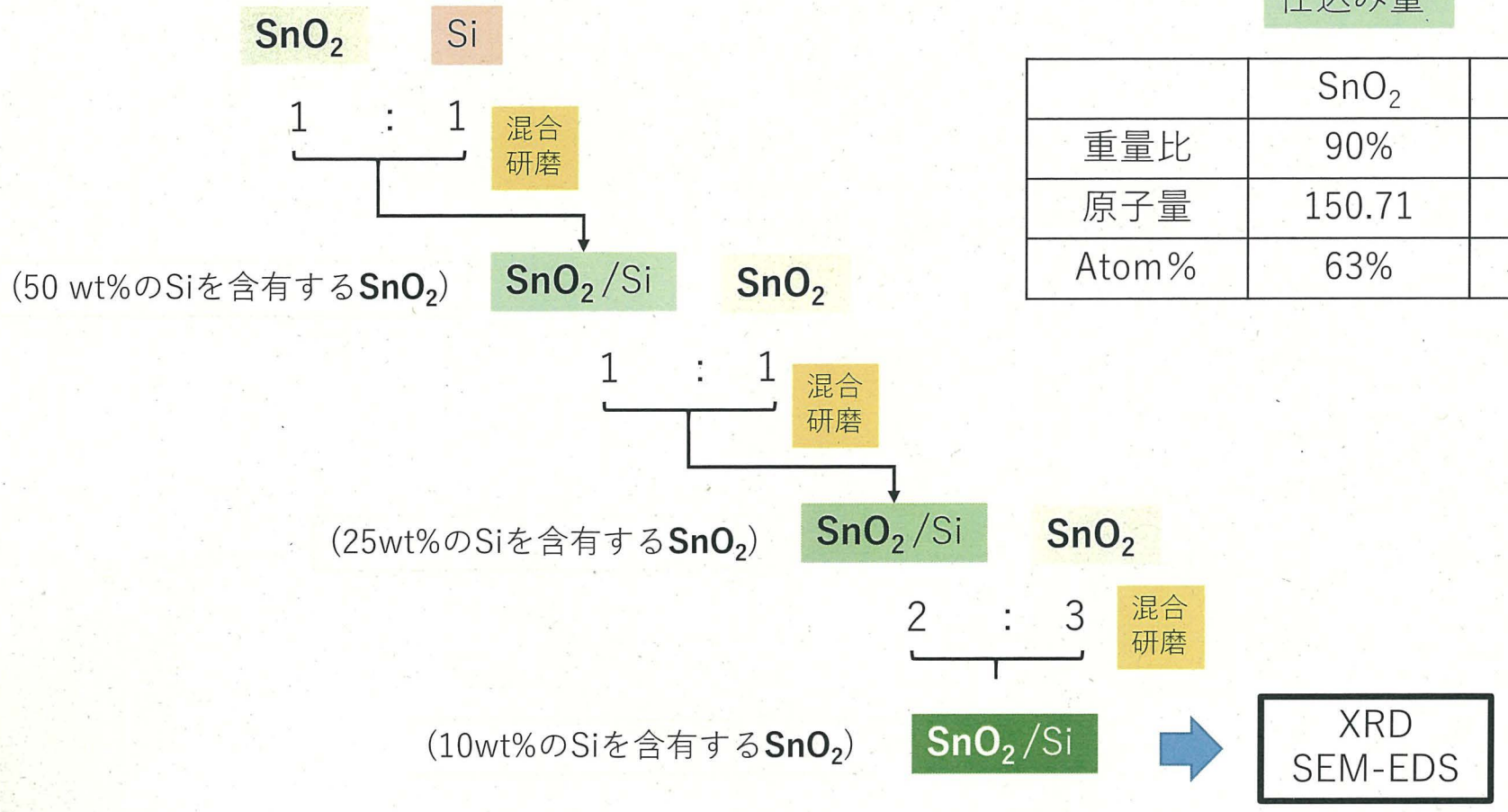

仕込み量

	SnO_2	Si
重量比	90%	10%
原子量	150.71	28.09
Atom%	63%	37%

SnO2の850°C焼成(市販)

XRD

sample	XRD(wt%)	
	SnO_2	Si
1	86.72	13.28
2	88.55	11.45
3	88.09	11.91

sample	XRD(wt%)		Atom(%)	
	SnO_2(Crys)	SnO_2(Amor)	SnO_2	Si
1	72.6	27.4	55	45
2	85.9	14.1	59	41
3	82.1	17.9	58	42

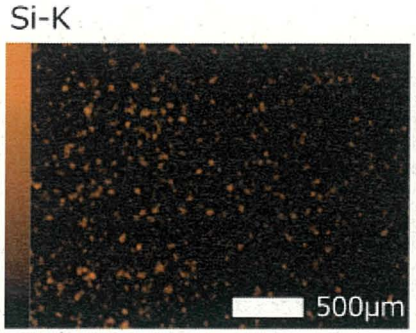

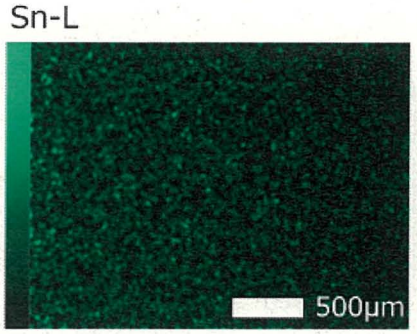

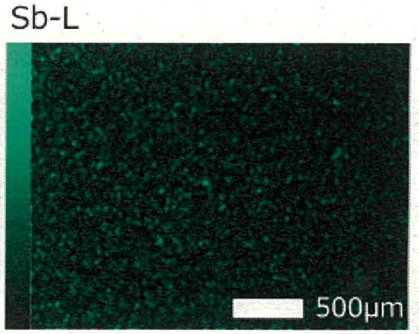

SEM

sample	Atom(%)	
	SnO_2	Si
1	57	43
2	56	44
3	61	39

SnO2の600°C焼成

XRD

sample	XRD(wt%)	
	SnO_2	Si
1	85.24	14.76
2	84.65	15.35
3	85.37	14.63

sample	XRD(wt%)		Atom(%)	
	SnO_2(Crys)	SnO_2(Amor)	SnO_2	Si
1	64.2	35.8	52	48
2	61.2	38.8	51	49
3	64.9	35.1	52	48

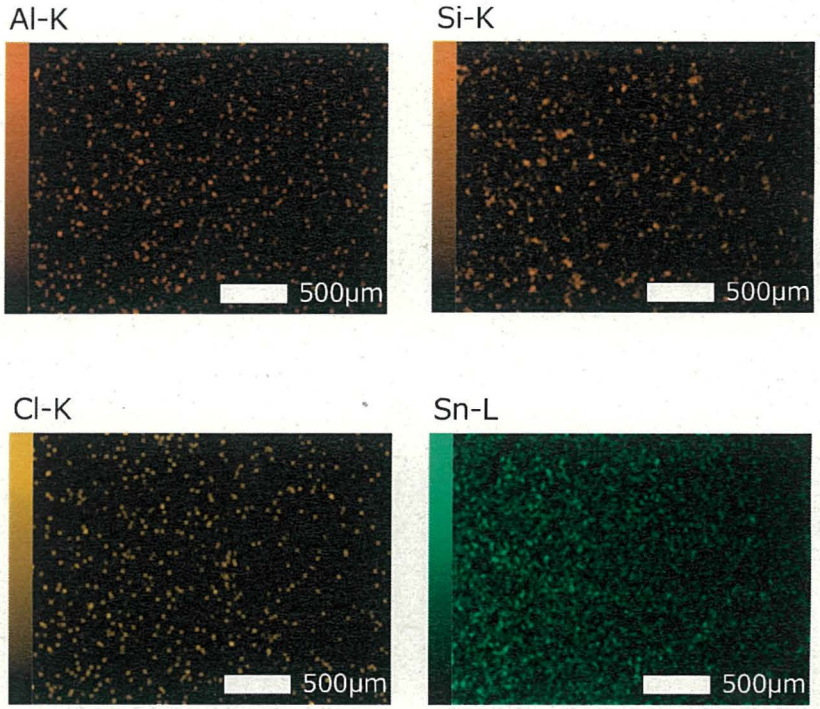

SEM

sample	Atom(%)	
	SnO_2	Si
1	65	35
2	65	35
3	65	35

SnO2の400°C焼成

XRD

sample	XRD(wt%)	
	SnO_2	Si
1	86.61	13.39
2	86.56	13.44
3	86.28	13.72

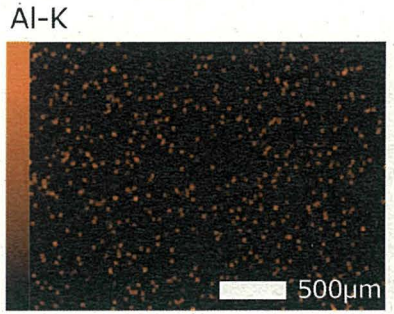

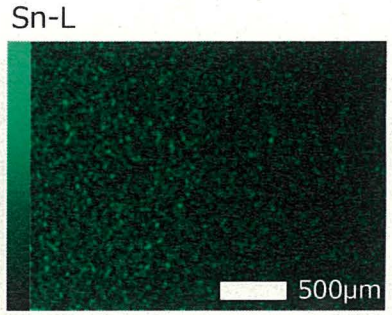

SEM

sample	XRD(wt%)		Atom(%)	
	SnO_2(Crys)	SnO_2(Amor)	SnO_2	Si
1	71.9	28.1	55	45
2	71.6	28.4	55	45
3	69.9	30.1	54	46

sample	Atom(%)	
	SnO_2	Si
1	70	30
2	73	27
3	63	37
4	66	34

SnO2の乾燥粉末(dry)

XRD

sample	XRD(wt%)	
	SnO_2	Si
1	93.19	6.81
2	92.48	7.52
3	92.16	7.84

sample	XRD(wt%)		Atom(%)	
	SnO_2(Crys)	SnO_2(Amor)	SnO_2	Si
1	-	-	72	28
2	-	-	70	30
3	-	-	69	31

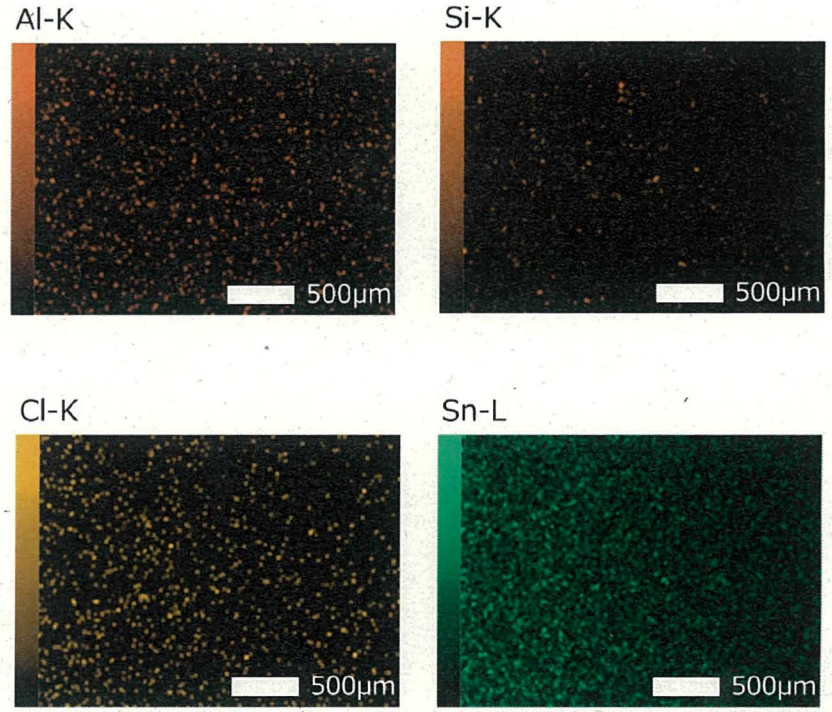

SEM

sample	Atom(%)	
	SnO_2	Si
1	88	12
2	88	12
3	84	16

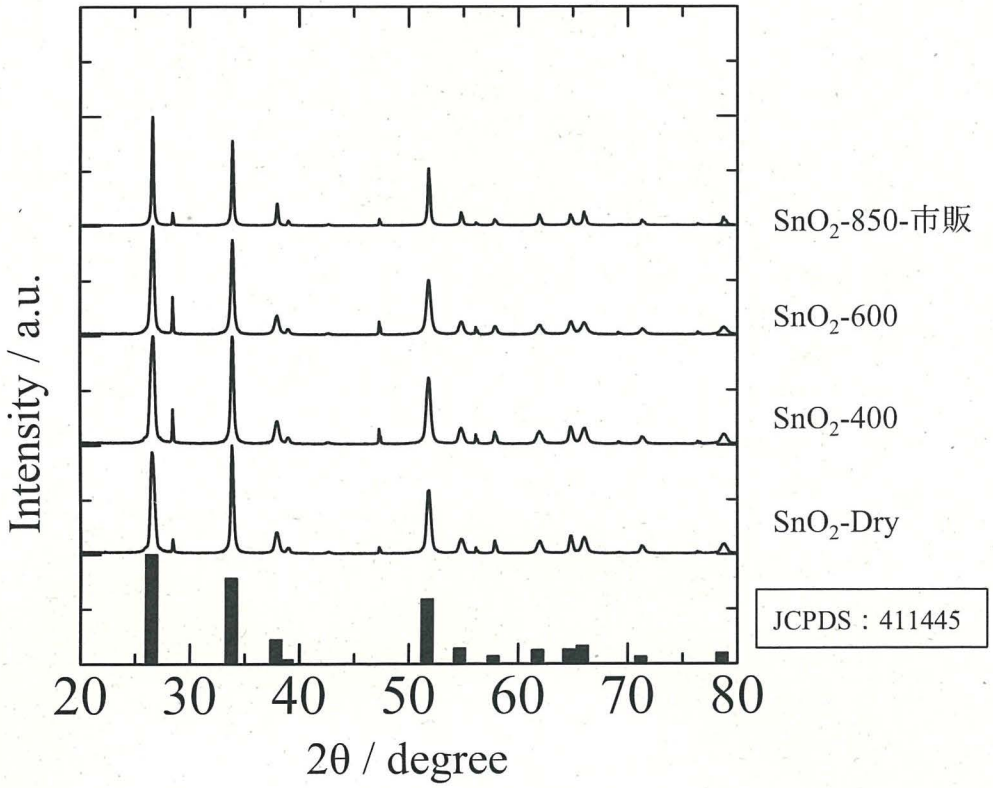
Intensity / a.u.
SnO2-850-市販
SnO2-600
SnO2-400
SnO2-Dry
JCPDS：411445
20 30 40 50 60 70 80
2θ / degree

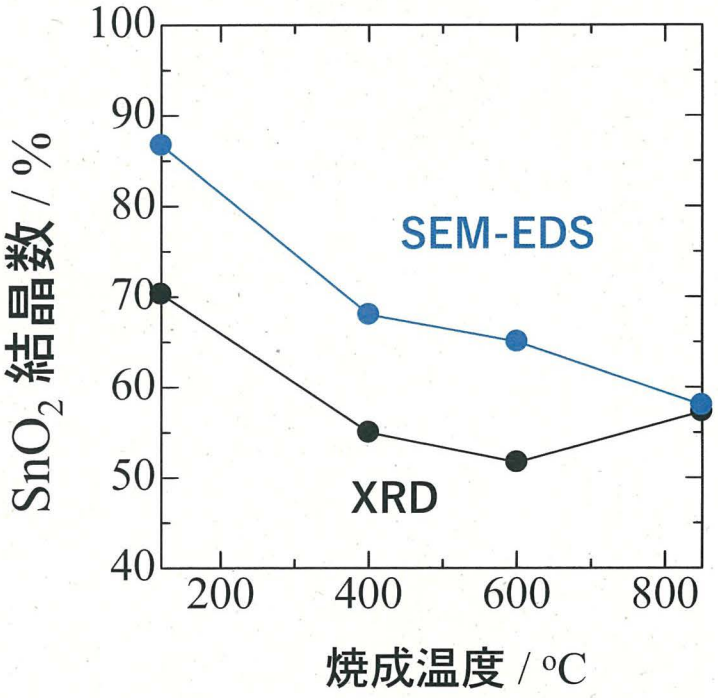
SnO2 結晶数 / %
100
90
80
70
60
50
40
SEM-EDS
XRD
200 400 600 800
焼成温度 / °C

焼成温度によるセンサ感度への影響